LITHOS 456–457 (2023) 107311

Contents lists available at ScienceDirect

LITHOS

journal homepage: www.elsevier.com/locate/lithos

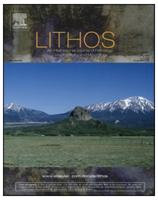

Magmatic evolution during proto-oceanic rifting at Alu, Dalafilla and Borale Volcanoes (Afar) determined by trace element and Sr-Nd-Pb isotope geochemistry

Emma J. Watts[a,*], Thomas M. Gernon[a], Rex N. Taylor[a], Derek Keir[a,b], Carolina Pagli[c]

[a] *School of Ocean and Earth Science, University of Southampton, European Way, Southampton SO14 3ZH, UK*
[b] *Dipartimento di Scienze della Terra, Università degli Studi di Firenze, Firenze 50121, Italy*
[c] *Dipartimento di Scienze della Terra, Università di Pisa, Pisa 56126, Italy*

ARTICLE INFO

Keywords:
Radiogenic-isotope
Trace-elements
Volcanic-plumbing-system
Continental-rifting

ABSTRACT

Continental rifting and associated magmatism can eventually result in the formation of new ocean basins. However, the characteristics of magmatism in the latest stages of rifting are poorly understood. The Erta-Ale volcanic segment (EAVS) in the Danakil Depression of Afar, Ethiopia, provides a unique natural laboratory in which to investigate how magma generation evolves during the shift from continental rifting to oceanic spreading. Here we present new trace element data combined with Sr-Nd-Pb isotope ratios for three volcanoes, Alu, Dalafilla and Borale, in the north of the EAVS. These data shed light on the changes in melt production and storage that occur at this late stage in the rifting cycle. Elevated Ce/Pb and ΔNb (33–48, 0.25–0.47 respectively) of the basalts, alongside Sr-Nd-Pb isotope geochemistry indicate the presence of a HIMU component, supplied by the Afar plume, together with contamination by the crust. Melting conditions, estimated using the trace element ratios, Sm_n/Yb_n, Dy_n/Yb_n and Ce_n/Sm_n, indicate that magmas were primarily derived from spinel lherzolite (85–90%) with minor garnet lherzolite (10–15%) with a melt fraction of ~4%. Melt-mantle equilibrium depths are estimated to be on the order of 64 to 83 km, shallower than that previously inferred within Afar. We suggest that this is likely a result of the increased plate thinning beneath the EAVS compared to other parts of Afar. Basaltic volcanics are found to exhibit heterogeneous Sr-Nd-Pb isotope compositions whilst more evolved rocks (i.e., $SiO_2 \geq 52$ wt%) exhibit consistent radiogenic compositions. This indicates that homogenisation of all melt compositions occurs prior to or during melt differentiation, with the latter process occurring rapidly in the upper crust with minimal crustal contamination. Overall whilst the Afar plume appears to be the dominant mantle component in the volcanic rocks, the melt characteristics and magmatic storage conditions beneath the EAVS shows variability that is likely controlled by a dynamic interplay between rifting and mantle processes.

1. Introduction

Afar is located at the northern end of the East African Rift (Fig. 1) and presents an opportunity to investigate the characteristics of volcanism within a plume-associated late-stage continental rift. This region has undergone extensive lithospheric thinning, as indicated by the high ratio of crustal thickness prior to rifting and crustal thickness currently observed (stretching factor (β) of 1.7–3) (Bastow and Keir, 2011; Maguire et al., 2006), resulting in low topography. The Danakil Depression in the northern part of Afar (Fig. 1) is the most advanced rift sector. Plate thinning is sufficiently high to have caused subsidence of the basin floor ~50–100 m below sea level, but it remains subaerial.

The Afar Depression is surrounded by the Ethiopian Plateau to the west, Somalian Plateau to the south, the Danakil block to the northeast, and the Ali-Sebeih block to the southeast (Hofstetter and Beyth, 2003). Afar lies on the triple junction of three major rifts which opened diachronously (Fig. 1): the Gulf of Aden (c. 35 million years ago, Ma); the Red Sea Rift (~29 Ma), and the Main Ethiopian Rift (MER, 18–15 Ma) (Leroy et al., 2012; Wolfenden et al., 2004). The depth to the Mohorovičić Discontinuity (Moho) is inversely related to the degree of extension (Hutchison et al., 2018), with the crustal thickness varying from 35 to 40 km in the MER to 15–16 km beneath the Danakil Depression in northern Afar (Chambers et al., 2019; Makris and Ginzburg, 1987).

---

* Corresponding author.
E-mail address: e.watts@soton.ac.uk (E.J. Watts).

https://doi.org/10.1016/j.lithos.2023.107311
Received 16 February 2023; Received in revised form 1 August 2023; Accepted 3 August 2023

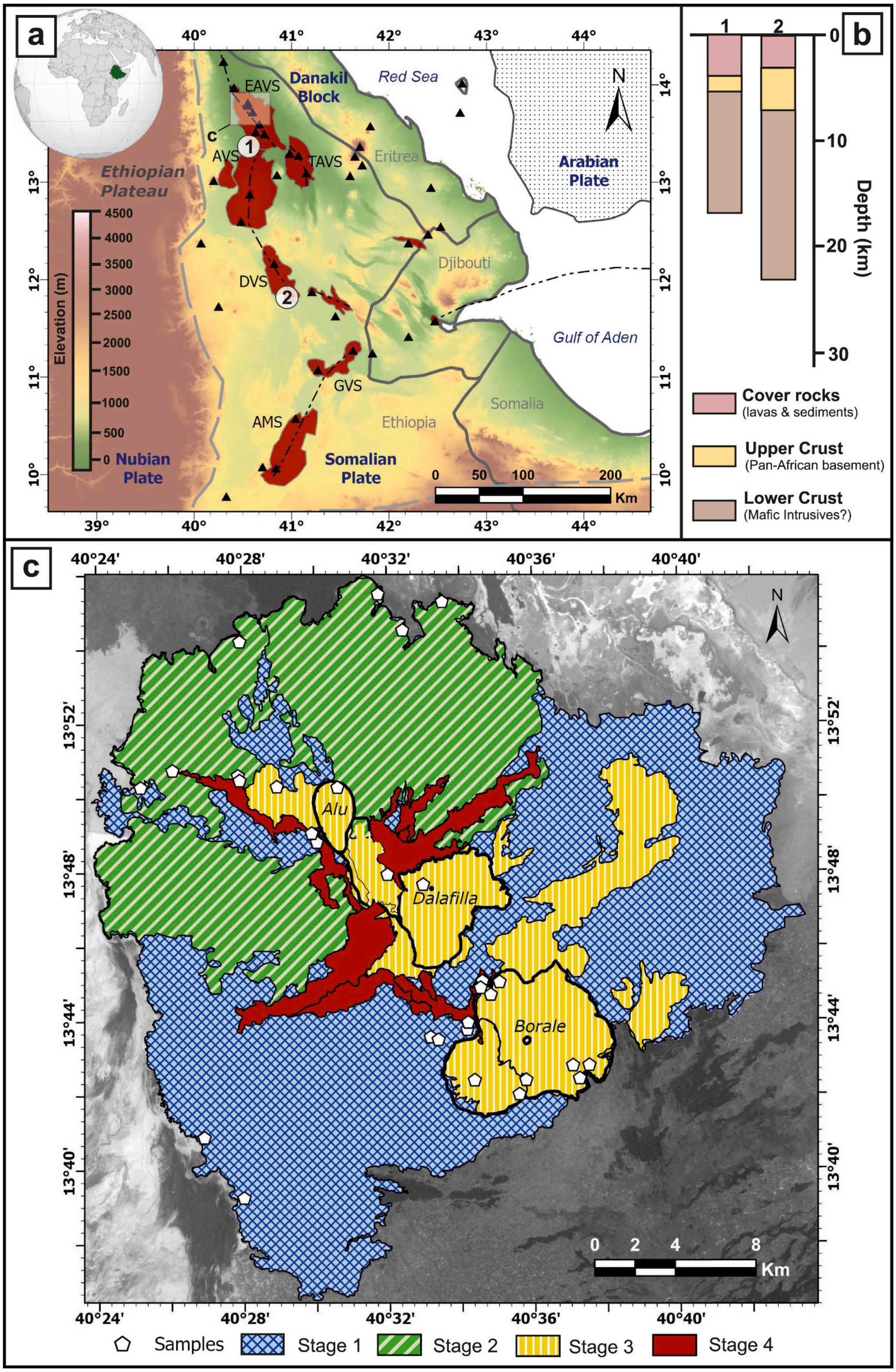

Fig. 1. (a) Afar region, Ethiopia. Black dashed lines indicate the rift zones. The study area is shown by the translucent box (labelled c). A more detailed view can be seen in panel (c). Volcanic segments are shown in red; the abbreviations from north to south are as follows: Erta Ale Volcanic Segment (EAVS), Afdera Volcanic Segment (AVS), Tat Ali Volcanic Segment (TAVS), Dabbahu Volcanic Segment (DVS), Gabilema Volcanic Segment (GVS), and the Adda'do Magmatic Segment (AMS). Numbers represent the locations of the crustal thickness profiles of (b). (b) Profiles showing the thicknesses of cover rocks, upper crust, and lower crust across two locations in Afar (locations shown in panel a). Figure modified after Hutchison et al. (2018). (c) Map of the north of the Erta Ale Volcanic Segment. The outline of the three volcanic centres (Alu, Dalafilla and Borale) are shown by thick black line. Sample locations are shown by the white pentagons. The deposits from the four stages of volcanic evolution are shown as follows: Stage 1: blue crosshatch, Stage 2: green diagonal lines. Stage 3: yellow vertical lines and Stage 4: solid red (Watts et al., 2020). See Section 2 for a summary of each of these stages. Imagery is Landsat 8 Panchromatic, sourced from the United States Geological Survey (USGS). (For interpretation of the references to colour in this figure legend, the reader is referred to the web version of this article.)

Volcanism in Afar began at approximately 31 Ma with the emplacement of Ethiopian Flood Basalts continuing until ∼29 Ma and erupting an estimated volume of ∼1 million km^3 of lava (Hofmann et al., 1997). The onset of volcanism in the area coincided closely with the initiation of Red Sea rifting between the Nubian Plate and the Arabian Plate (Ebinger et al., 2008). This resulted in coeval flood basalts being emplaced in both Ethiopia and Yemen, currently separated by the Red Sea (Wolfenden et al., 2005). Volcanic activity has persisted in the area since this time, with progressive emplacement of the: Mablas rhyolites and basalts at 15–10 Ma, the Dahla series at 9–4 Ma (Vidal et al., 1991) and more recently (3.5–0.6 Ma) the Stratoid Series (Lahitte et al., 2003; Tortelli et al., 2022). Since 0.6 Ma, volcanism across the Afar region has been concentrated at volcanic segments (Barberi and Varet, 1970), with a current rate of rifting between the Arabian and Nubian Plates at the Erta-Ale Volcanic Segment (EAVS) ∼14 mm/yr (Fig. 1) (Viltres et al., 2020).

Regional geochemical investigations of volcanism are available across Afar and the Main Ethiopian Rift (Hutchison et al., 2018; Rooney, 2017, 2020a, 2020b, 2020c), in addition to localised studies carried out for volcanic centres across Afar (Barrat et al., 1998; Ferguson et al., 2013; Field et al., 2012; Field et al., 2013; Medynski et al., 2013; Medynski et al., 2015; Tortelli et al., 2021). However, geochemical data relating to volcanism within the Danakil Depression, especially at high spatial resolution, is limited. As a result, spatial and temporal changes in magma production and transport in this setting are unclear.

Geochemical methods have indicated a large range for the depth of melting across the region, with the Dabbahu volcanic segment (DVS), central-north Afar, showing evidence for melt generation at depths of >80 km (Ferguson et al., 2013), and basalts from the Ethiopian Plateau providing shallower estimates of 30–60 km (Ayalew et al., 2018). For context, melt generation depth estimates from the northern MER are ∼110 km (Chiasera et al., 2018; Chiasera et al., 2021). This range of melting depths across the wider region suggests that the depth of melting varies as rifting progresses, but data are lacking in northern Afar to rigorously test this hypothesis.

The focus of this study is three volcanoes, Alu, Dalafilla and Borale, situated within the EAVS, a volcanic segment within the Danakil Depression (Fig. 1). Although current access to the EAVS is limited, due to political instability, a fissure eruption to the southeast of Alu was observed via satellite in 2008 (Pagli et al., 2012). Watts et al. (2020) mapped and produced a relative chronology of the three volcanoes using Landsat 8 and ASTER data alongside petrological and geochemical data (see section 2 for more details).

This paper presents new Sr-Nd-Pb isotope compositional data alongside trace element data for the Alu, Dalafilla, and Borale volcanoes. The aim of this paper is to utilise these new data to further understand magma production and transport at volcanoes within a plume-influenced rift setting. Our specific objectives are to (1) use Sr-Nd-Pb isotopes to identify the mantle source and crustal components; (2) use trace element modelling to constrain the depth of melting and melt fraction; and (3) use Sr-Nd-Pb to help constrain the pathway of the magma from source to eruption. We integrate the results with the previous geospatial work of Watts et al. (2020) to provide new detailed geochemical insights into the melt generation and pathways within Alu, Dalafilla, and Borale.

2. Alu, Dalafilla and Borale volcanoes

The EAVS is a volcanic ridge comprised of lava flows, evaporites and clastic sediments (Barberi and Varet, 1970). Lalou et al. (1970) dated the marine reef deposits on the western edge of the Danakil Depression associated with Red Sea flooding events (c. 200 kyr, 120 kyr and 80 kyr). Watts et al. (2020) use the lack of visible corals in the region to indicate the age of the subaerial deposits within the EAVS, and hence Alu, Dalafilla and Borale volcanoes, are mostly post-desiccation (<80 kyr).

Dalafilla and Borale are stratovolcanoes (elevation 578 m and 625 m respectively) and Alu, in the north of the study area (Fig. 1c) is an ellipsoidal dome elongated NNW-SSE. Watts et al. (2020) identified 92 lava flows (excluding the oldest rift floor lavas), which were classified into 15 phases of eruptive activity. Based on their eruptive characteristics and major element composition, these 15 phases were then grouped into 4 main stages that signify the main stages of volcanic evolution over time (Fig. 1c). Watts et al. (2020) describes each of the stages as follows: Stage 1 (rift floor basalts) comprises widespread, highly weathered blanket-like lava flows that occur across the whole study area. Later flows within this stage were erupted from fissures around Borale and Alu. Stage 2 (fissure lavas) is characterised by extensive flows originating from fissures with volcanic activity migrating clockwise around Dalafilla and Alu. Stage 3 is characterised by volcanic products erupted from each volcanic edifice, rather than the flanks. Stage 4 (rejuvenated fissures) includes low-volume flows originating from fissures on the flanks of the volcanoes. The most recent flow of this stage was erupted in 2008 (Pagli et al., 2012). To our knowledge, no radiometric dates for the volcanic products within the study area have been published.

The 30 samples within this study are those analysed within Watts et al. (2020) and for ease of comparison investigated lavas hereafter follow the same grouping scheme, with the stage and rock classification of each sample shown in Table 1.

All samples are tholeiitic, lying below the tholeiitic/alkaline boundary, but show a mild alkaline affinity (Fig. 2; Watts et al., 2020). Lavas from Stages 1 and 2 are basalts (Table 1, Fig. 2) and are clustered with similar major element concentrations observed. Samples from Stage 3, erupted from the volcanic edifices, show a wider range in compositions varying from basaltic-trachy-andesite to rhyolite (Table 1, Fig. 2). Stage 4 is bimodal, with the older lava flows being of basaltic-andesite composition and the younger flows being basaltic in composition.

Watts et al. (2020) modelled the compositional evolution of these events and proposed that they formed via fractional crystallisation alone, with negligible crustal assimilation occurring during this process.

Table 1
Sample numbers, coordinates, rock-types (based on the TAS classification; LeBas et al., 1986), and stage of volcanic evolution according to Watts et al. (2020).

Sample ID	Latitude	Longitude	Rock type	Stage
D152	13.7295	40.5694	Basalt	1
G43	13.8386	40.4201	Basalt	1
G66	13.6815	40.4486	Basalt	1
G65	13.6544	40.4667	Basalt	1
D156	13.7069	40.5727	Basalt	1
M6	13.7263	40.5526	Basalt	1
M7	13.7251	40.5562	Basalt	1
D15	13.8384	40.5105	Basalt	1
F60	13.7992	40.5332	Basalt	1
CH21	13.8438	40.4648	Basalt	2
CH22	13.8416	40.4656	Basalt	2
F49	13.9039	40.4658	Basalt	2
D2	13.9250	40.5295	Basalt	2
D7	13.9087	40.5407	Basalt	2
D8	13.9215	40.5589	Basalt	2
D141	13.7005	40.5932	Pumice	3
CH20	13.8388	40.4826	Rhyolite	3
D137	13.7133	40.6178	Trachyte	3
D138	13.7075	40.6209	Trachyandesite	3
D140	13.7135	40.6253	Trachyte	3
D143	13.7069	40.5963	Trachyandesite	3
D147	13.7509	40.5843	Basaltic trachyandesite	3
D148	13.7452	40.5802	Trachyandesite	3
F59	13.7947	40.5495	Trachyte	3
CH23	13.8461	40.4348	Basaltic andesite	4
F54	13.8138	40.5009	Basaltic andesite	4
F55	13.8179	40.4985	Basaltic andesite	4
D149	13.7513	40.5765	Basalt	4
D150	13.7483	40.5756	Basalt	4
D153	13.7328	40.5698	Basalt	4

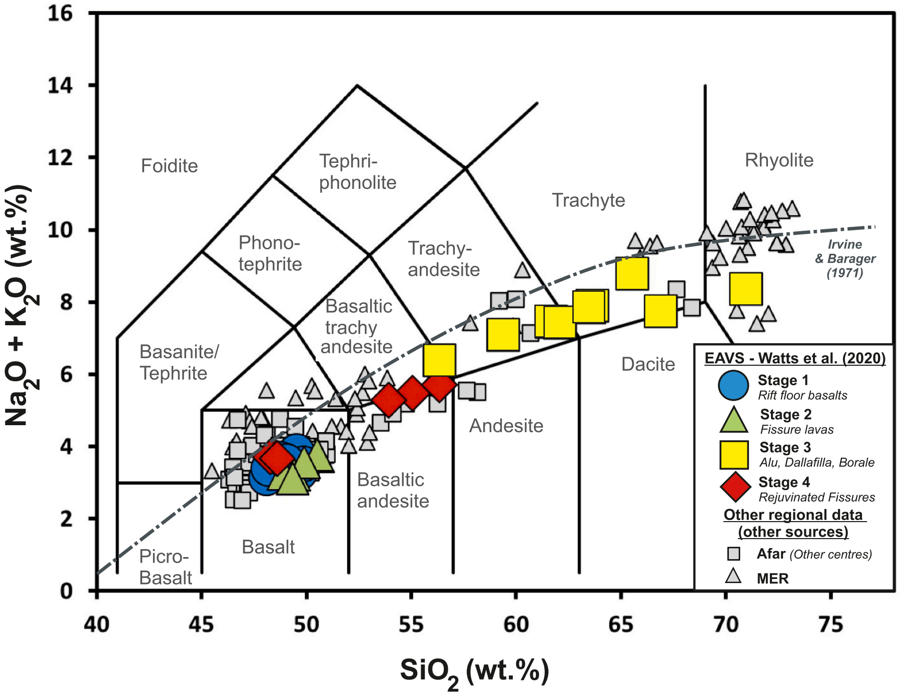

Fig. 2. Total Alkali-Silica diagram modified from Watts et al. (2020). Whole rock compositions of the samples within this study are displayed by the large symbols corresponding to the evolution stage: 1 = blue circle, 2 = green triangle, 3 = yellow square, 4 = red diamond. Small grey symbols show previously published whole rock compositions across Afar (squares) and MER (triangles). Dashed line shows the division of volcanic rocks into alkaline (above) and subalkaline/tholeiitic (below) after Irvine and Baragar (1971). (For interpretation of the references to colour in this figure legend, the reader is referred to the web version of this article.)

All samples contained phenocrysts of plagioclase and clinopyroxene with the basaltic and trachyte samples also containing olivine (< 4%) and orthopyroxene (<5.1%). Watts et al. (2020) also notes the presence of magnetite and apatite as accessory minerals in the groundmass. Three samples (D141, CH23, F55) were noted to lack phenocrysts.

3. Analytical methods

Thirty samples across the three volcanic centres (locations shown in Fig. 1 and coordinates in Table 1) were selected from the Afar repository (a publicly available collection, https://repositories.dst.unipi.it/index.php/home-afar) at the University of Pisa. Care was taken to ensure we selected a representative suite of rocks of different compositions and grain-sizes, with samples located away from the edges of the flows. The samples were collected during the CNR/CNRS projects in Afar during the 1960s (Barberi and Varet, 1970).

All samples were crushed and sieved to obtain rock chips of 0.5–1 mm grain size. The chips were subsequently washed in an ultrasonic bath for 3 h and dried in an oven at 85^0C for 24 h. Once dry, rock chip samples were picked under an optical microscope to target the freshest material and discard any contaminants. All sample preparation and subsequent analyses were carried out at the University of Southampton, UK.

For trace element analysis, an aliquot of rock chips was manually powdered in an agate pestle and mortar. The powdered samples underwent HF-HCl acid digestion and were subsequently diluted to 4000× dilution factor. All samples were run on a ThermoScientific XSeries2 quadrupole ICP-MS alongside international standards (JA-2, BHVO-2, JB-2, JB-1a, and BCR-2). Reproducibility errors were typically smaller than ±4%. Accuracy values are typically ≤6% with the exception of Cr, Cu, Ni.

For Pb isotopic analysis, rock chips initially underwent a 1 h leaching period in 6 M HCl, followed by $HF\text{-}HNO_3\text{-}HCl$ digestion. The samples were then centrifuged and the Pb isolated using the HCl-AG1x8 resin method (Kamber and Gladu, 2009). Next, the Pb isolate was dried down, redissolved in HNO_3 and analysed using the double spike method of Taylor et al. (2015). The samples were subsequently analysed on a ThermoScientific Neptune MC-ICP-MS at the University of Southampton (UK) with a NBS SRM 981 reproducibility of $^{206}Pb/^{204}Pb = 16.9404 \pm 32$, $^{207}Pb/^{204}Pb = 15.4969 \pm 32$, $^{208}Pb/^{204}Pb = 36.7149 \pm 90$ (2sd; $n = 40$). Accuracy values were < 1%.

20 of these samples were also analysed for $^{87}Sr/^{86}Sr$ and $^{143}Nd/^{144}Nd$. Here, all samples were passed through ion exchange column chemistry, using a AG50-X8 200–400 mesh resin cation column to separate the Sr and Nd fractions. Sr was further isolated through Sr-spec resin column, following the methodology of Pin et al. (1994). Samples were subsequently loaded on to degassed tantalum filaments and analysed on a ThermoScientific Triton Plus (TIMS). SRM NIST987 $^{87}Sr/^{86}Sr$ gave average values of 0.710243 and samples are quoted relative to 0.710248, while reproducibility was ±0.000020 (2sd; $n = 464$). Accuracy values were < 1%. Isotopic age correction for high Rb/Sr samples is considered negligible due to the inferred young age of the lavas (Watts et al., 2020). The Nd aliquot from the cation column was followed by an Ln-spec resin (50–100 μm). A solution of 50 ppb Nd was prepared and subsequently analysed on a ThermoScientific Neptune MC-ICP-MS, with SRM JNdi-1 producing an average $^{143}Nd/^{144}Nd$ of 0.512115 and samples are quoted relative to 0.512099, with a reproducibility of ±0.000006 (2sd) across 6 analysis sessions over 2 years. Accuracy values were < 1%.

4. Results

4.1. Trace elements

Selected trace elements are plotted against Zr to illustrate the effects of crystallisation (Fig. 3). Zr concentrations are in the range 176–856 ppm, with concentrations >300 ppm associated with the evolved samples (Stage 3 and the basaltic andesites of Stage 4; Tables 1 and 2). Y displays a strong positive correlation with Zr, indicating a negligible crystallisation of amphibole and apatite during differentiation (Fig. 3) and that is supported by the samples' petrology, major element compositions, and fractional crystallisation modelling previously undertaken by Watts et al. (2020).

The basalts (Stages 1, 2, and 4) have relatively high Sr contents (236–405 ppm), with lower Sr in the more evolved samples reflecting feldspar fractionation (hereafter we take the evolved samples to have Zr

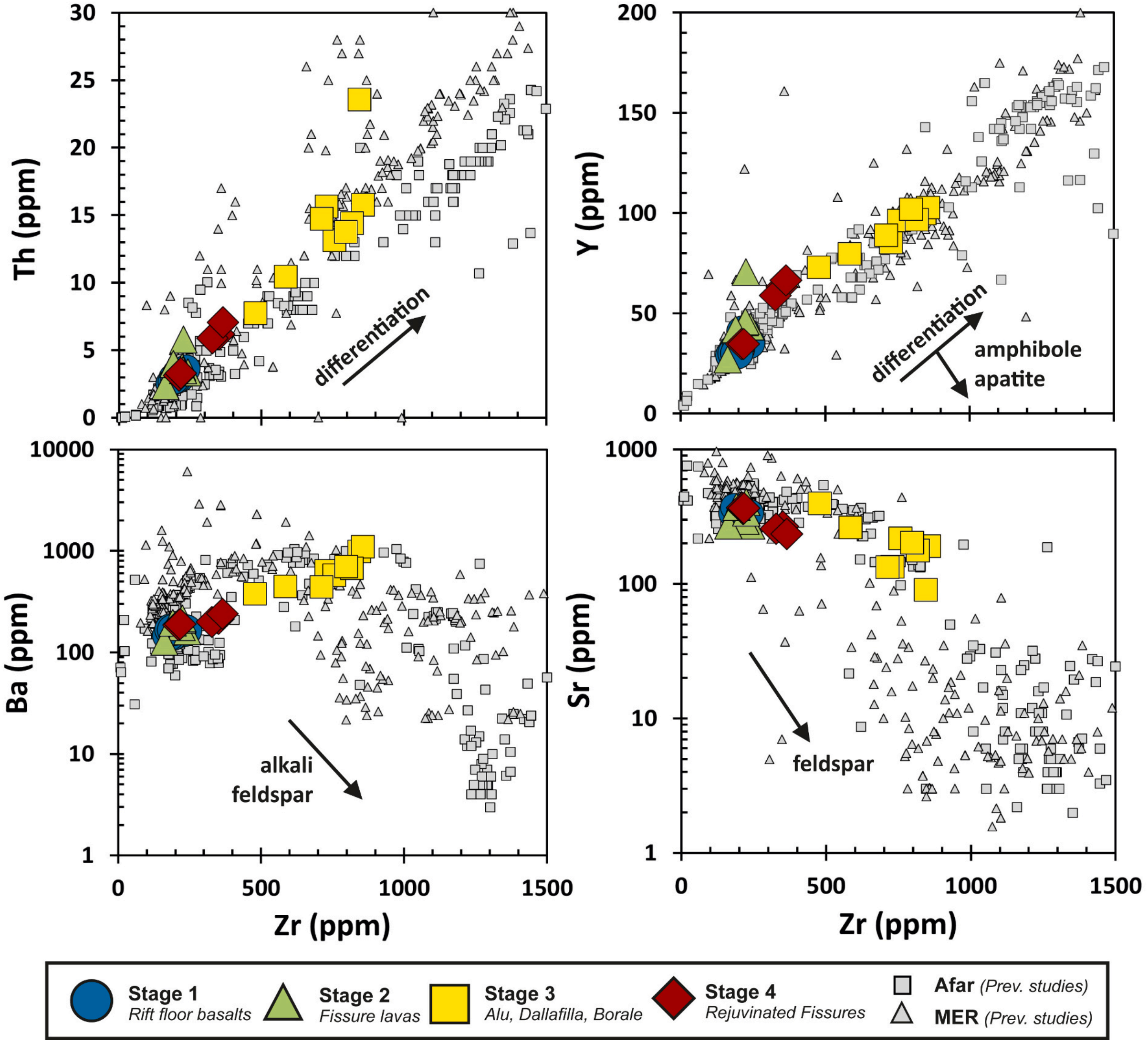

Fig. 3. Selected trace element compositions plotted against Zr concentration (ppm). The influence of magmatic differentiation and various crystallising mineral phases are represented by the black arrows. Symbols are as follows: blue (circle) is Stage 1, green (triangle) is Stage 2, yellow (square) is Stage 3, and red (diamond) is Stage 4. Representative data for Afar are shown by the grey squares and representative data for the MER are shown by grey triangles. Both fields were collated from previously published datasets downloaded from the GEOROC database (DIGIS, 2021; https://georoc.eu/) on 20th June 2022 (see S3 for references to studies included in the downloaded dataset). (For interpretation of the references to colour in this figure legend, the reader is referred to the web version of this article.)

>300 ppm and $SiO_2 > 52$ wt%; Fig. 3). Barium concentrations are in the range 130–1100 ppm, which is within the previously observed range for Afar. The progressive increase in Ba with Zr (Fig. 3) indicates that plagioclase rather than alkali feldspar is the dominant crystallising phase, re-enforcing the lack of alkali feldspar observed in these samples (Watts et al., 2020; Figs. 3 & 5).

Chondrite-normalised rare earth element (REE) patterns are sub-parallel for all four stages (Fig. 4a) and characterised by an enrichment in light-REE (LREE; $La_n/Sm_n \sim 2.5$, Fig. 5c), and a moderate enrichment in middle REE (MREE) relative to the heavy-REEs (HREE; $Dy_n/Yb_n \sim 1.4$, Fig. 5c). The REE patterns of Stage 1 and 2 basalts are broadly similar to that of the high-Ti-2 (HT2) basalts of the Ethiopian Plateau, though HT2 exhibits a steeper HREE depletion (Dy_n/Yb_n: 1.30–1.46; Pik et al., 1999). In general, the EAVS samples have a shallower HREE depletion compared to all basalts of the Ethiopian Plateau ($Dy_n/Yb_n \sim 1.6$, Fig. 5c; Pik et al., 1999).

The primitive mantle-normalised multi-element diagrams (Fig. 4b) again show a relatively similar pattern across all four stages of activity, with a generally progressive increase in normalised concentrations towards the highly incompatible elements. Basaltic samples are characterised by low values of Cs, Rb, Ba, Sr and Pb and relatively high values of Nb, Ta. All lavas are depleted in Ba, Pb and Sr (Fig. 4b).

The evolved samples within Stages 3 and 4 have substantial negative Eu/Eu* anomalies (0.62–0.95 and 0.85–0.88 respectively; Fig. 4a), whereas the basalts (Stages 1, 2, and 4) have negligible Eu anomalies (Eq. 1: $Eu/Eu^* = Eu_n/(Sm_n \times Gd_n)^{0.5}$; 0.95–1.02, Fig. 5a). All samples have a negative Sr anomaly (Eq. 2: $Sr/Sr^* = Sr_n/(Nd_n \times Pr_n)^{0.5}$) with Stage 1, 2 and 4 basalts in the range 0.47–0.77 (Fig. 5a), Stage 4 basaltic andesites 0.24–0.31 (Fig. 5a), and Stage 3 having the most negative anomalies with 0.06–0.3 (Fig. 5a). Stages 3 and 4 also exhibit relative depletions in both Eu and Ti, whereas Stages 1 and 2 only show enrichment in Ti. Stage 3 lavas have a relative enrichment in Zr and Hf.

All samples have Ce/Pb between 29.7 and 48.0 (Fig. 5b), which is higher than typical MORB (i.e., calculated from Atlantic, Pacific, and Indian Oceans, which is 25 ± 5; Hofmann et al., 1986). Correspondingly, all samples also have positive ΔNb (Eq. 3: $\Delta Nb = 1.74 + \log(Nb/Y) - (1.92 \times \log(Zr/Y))$; Fitton et al., 1997) in the range 0.09–0.47, with basalts exhibiting the highest ΔNb.

Table 2
Trace element and Pb-Sr-Nd isotope results for samples from the Alu, Dalafilla and Borale volcanoes (refer to Table 1 for coordinates and rock types).

	Stage 1						
Sample ID	D152	G43	G66	G65	D156	M6	M7
Trace elements (ppm)							
Li	3.98	5.28	5.20	5.15	4.83	4.04	4.30
Sc	39.9	36.4	35.6	34.8	33.6	36.0	34.7
Ti	17,790	17,270	17,330	15,670	14,180	15,720	15,520
V	408	411	387	352	340	361	349
Cr	112	7	11	235	21	301	164
Co	40.1	44.8	42.8	44.6	37.7	46.1	36.5
Ni	42.3	30.6	28.4	102.8	31.1	125.5	59.7
Cu	126.9	110.8	96.7	100.0	160.4	84.5	85.2
Zn	110.0	110.6	108.0	99.3	97.1	98.1	91.6
Rb	13.6	14.3	14.0	13.9	11.9	12.2	13.5
Sr	290	323	336	352	320	336	374
Y	41.1	34.0	35.5	32.7	32.0	29.3	30.3
Zr	214	210	235	199	187	176	183
Nb	36.0	40.6	43.4	35.8	33.2	34.1	39.5
Cs	0.133	0.183	0.143	0.138	0.124	0.123	0.136
Ba	162	159	166	164	149	149	169
La	26.4	29.2	31.0	26.1	25.7	24.0	26.5
Ce	58.8	63.6	67.6	56.3	55.2	52.3	57.3
Pr	7.6	8.0	8.5	7.1	7.1	6.6	7.2
Nd	32.4	33.1	34.7	29.5	29.0	27.5	29.7
Sm	7.52	7.14	7.43	6.51	6.44	6.06	6.44
Eu	2.44	2.32	2.34	2.15	2.06	2.02	2.15
Gd	7.84	7.00	7.36	6.56	6.40	6.06	6.36
Tb	1.237	1.087	1.133	1.015	1.009	0.942	0.980
Dy	7.45	6.31	6.62	5.98	5.82	5.42	5.65
Ho	1.48	1.24	1.27	1.17	1.16	1.06	1.11
Er	4.10	3.32	3.46	3.20	3.14	2.83	2.98
Tm	0.585	0.470	0.490	0.456	0.449	0.402	0.418
Yb	3.73	2.89	3.06	2.85	2.81	2.49	2.61
Lu	0.546	0.432	0.442	0.426	0.414	0.370	0.386
Hf	5.29	5.05	5.55	4.75	4.57	4.24	4.32
Ta	2.215	2.443	2.626	2.256	2.036	2.120	2.445
Pb	1.37	1.60	1.58	1.43	1.47	1.39	1.43
Th	2.95	3.22	3.65	2.81	2.99	2.54	2.68
U	0.792	0.852	0.952	0.762	0.765	0.693	0.744
Isotopes							
$^{87}Sr/^{86}Sr$	0.703598	0.703695	0.703715		0.703599		0.703515
2SE	12.6	6.5	6.7		6.1		6.7
$^{143}Nd/^{144}Nd$	0.512937	0.512902	0.512918	0.512922	0.512916		
2SE	24	5	5	6	5		
$^{206}Pb/^{204}Pb$	19.02	19.16	19.14	19.05	19.10	19.13	19.33
$^{207}Pb/^{204}Pb$	15.582	15.599	15.594	15.560	15.591	15.596	15.603
$^{208}Pb/^{204}Pb$	38.98	39.16	39.15	39.04	39.10	39.11	39.25

	Stage 1		Stage 2				
Sample ID	D15	F60	CH21	CH22	F49	D2	D7
Trace elements (ppm)							
Li	7.90	4.91	6.31	9.67	4.36	10.23	13.03
Sc	56.6	34.8	34.7	57.2	33.3	108.1	82.4
Ti	15,070	14,690	18,050	17,130	13,150	14,880	18,780
V	383	360	464	443	355	386	403
Cr	18	30	18	17	28	28	22
Co	46.2	43.7	47.8	45.7	43.9	49.6	43.9
Ni	29.9	41.5	34.4	31.7	35.1	37.7	25.3
Cu	88.3	122.8	143.4	133.9	95.5	98.5	95.8
Zn	104.0	98.8	122.5	120.4	93.3	108.7	126.5
Rb	14.0	13.5	9.8	17.8	9.6	17.6	24.7
Sr	322	292	270	296	271	406	340
Y	34.6	30.2	43.4	45.5	27.0	70.7	46.0
Zr	201	193	241	221	162	225	225
Nb	36.7	37.8	41.9	40.1	31.2	35.3	39.2
Cs	0.121	0.131	0.085	0.193	0.094	0.179	0.310
Ba	170	168	161	178	127	210	217
La	26.5	26.5	30.1	29.2	22.1	30.9	29.5
Ce	55.8	57.4	64.6	61.9	47.8	67.1	64.0
Pr	7.1	7.2	8.2	7.9	6.0	8.6	8.2
Nd	29.2	29.7	34.0	32.9	24.8	35.8	34.7
Sm	6.49	6.39	7.73	7.46	5.54	8.62	7.95

(*continued on next page*)

Table 2 (*continued*)

	Stage 1		Stage 2				
Sample ID	D15	F60	CH21	CH22	F49	D2	D7
Eu	2.11	2.07	2.47	2.40	1.81	2.93	2.56
Gd	6.66	6.41	8.08	7.90	5.60	9.39	8.29
Tb	1.044	1.003	1.283	1.262	0.886	1.469	1.312
Dy	6.09	5.83	7.66	7.48	5.20	8.66	7.76
Ho	1.21	1.15	1.55	1.52	1.04	1.72	1.56
Er	3.31	3.14	4.28	4.17	2.82	4.71	4.24
Tm	0.478	0.447	0.624	0.609	0.405	0.680	0.607
Yb	2.98	2.76	3.89	3.86	2.53	4.45	3.83
Lu	0.433	0.405	0.573	0.569	0.367	0.668	0.561
Hf	4.80	4.65	5.74	5.30	4.02	5.21	5.37
Ta	2.297	2.254	2.681	2.491	1.923	2.356	2.508
Pb	1.41	1.73	1.65	1.56	1.46	1.59	1.80
Th	3.32	2.81	3.36	3.74	2.36	5.79	3.53
U	0.802	0.841	0.867	0.834	0.714	0.835	0.775
Isotopes							
^{87}Sr/^{86}Sr	0.703635	0.703691	0.703709	0.703629		0.703898	0.703650
2SE	6.7	6.6	5.8	6.7		6.8	5.8
^{143}Nd/^{144}Nd	0.512908	0.512899			0.512921	0.512893	0.512907
2SE	6	5			5	5	5
^{206}Pb/^{204}Pb	19.19	19.24	19.12	18.91	19.19	19.19	19.06
^{207}Pb/^{204}Pb	15.600	15.600	15.599	15.595	15.599	15.598	15.591
^{208}Pb/^{204}Pb	39.14	39.20	39.09	38.86	39.14	39.14	39.05

	Stage 2	Stage 3					
Sample ID	D8	D141	CH20	D137	D138	D140	D143
Trace elements (ppm)							
Li	9.18	16.97	19.89	18.15	14.82	17.24	10.36
Sc	82.3	10.0	27.3	26.1	19.3	16.8	20.2
Ti	13,790	3492	3999	8908	11,030	8641	11,870
V	374	9	7	24	55	24	59
Cr	59	0	1	1	2	0	2
Co	48.3	1.7	1.5	7.2	10.1	7.0	10.2
Ni	46.9	0.2	0.3	0.6	1.4	0.5	1.6
Cu	108.1	5.1	5.4	16.8	18.5	15.8	20.4
Zn	99.3	105.3	91.1	160.2	164.5	156.7	172.1
Rb	18.0	74.6	169.7	108.1	62.7	73.7	76.4
Sr	374	135	91	191	218	177	203
Y	42.2	85.2	99.8	102.7	96.4	96.7	101.9
Zr	190	728	844	856	756	817	797
Nb	33.3	120.5	137.0	147.1	137.8	143.8	146.5
Cs	0.191	0.752	0.793	0.750	0.661	0.727	0.640
Ba	196	636	990	1096	576	673	703
La	26.2	85.0	96.9	102.2	100.9	102.7	104.5
Ce	54.7	162.7	187.4	207.8	194.6	197.5	201.3
Pr	6.9	20.0	22.7	26.1	24.6	24.8	25.3
Nd	28.6	74.3	84.1	99.5	94.9	94.5	98.0
Sm	6.49	14.74	16.68	19.94	19.20	18.78	19.60
Eu	2.14	3.16	3.32	4.92	4.81	4.60	4.81
Gd	6.74	13.87	15.64	18.44	17.98	17.45	18.41
Tb	1.067	2.304	2.604	2.979	2.846	2.798	2.934
Dy	6.26	13.90	15.97	17.54	16.64	16.50	17.29
Ho	1.26	2.83	3.32	3.51	3.30	3.31	3.42
Er	3.44	8.24	9.65	9.84	9.21	9.25	9.51
Tm	0.494	1.262	1.490	1.459	1.361	1.371	1.405
Yb	3.16	8.25	9.83	9.27	8.58	8.73	8.86
Lu	0.466	1.221	1.479	1.378	1.261	1.288	1.308
Hf	4.50	17.46	21.55	20.36	17.84	19.03	18.64
Ta	2.155	6.392	10.110	9.370	8.054	8.265	8.226
Pb	1.84	5.15	5.02	5.77	5.31	5.59	5.33
Th	3.97	15.66	23.58	15.78	13.15	14.42	13.77
U	0.780	3.842	4.834	3.884	3.408	3.668	3.402
Isotopes							
^{87}Sr/^{86}Sr	0.703884	NA	0.703841	0.703634	NA	0.703635	0.703634
2SE	6.7		33.3	6.3		10.6	6.5
^{143}Nd/^{144}Nd	0.512892	0.512903	0.512892	0.512903	0.512896	0.512883	0.512898
2SE	4	5	6	5	6	5	5
^{206}Pb/^{204}Pb	19.18	19.11	19.12	19.09	19.10	19.10	19.10
^{207}Pb/^{204}Pb	15.600	15.592	15.597	15.589	15.591	15.591	15.591

(*continued on next page*)

Table 2 (*continued*)

	Stage 2	Stage 3					
Sample ID	D8	D141	CH20	D137	D138	D140	D143
^{208}Pb/^{204}Pb	39.14	39.07	39.09	39.09	39.10	39.10	39.10

	Stage 3			Stage 4			
Sample ID	D147	D148	F59	CH23	F54	F55	D149
Trace elements (ppm)							
Li	10.85	12.43	16.89	8.94	7.94	8.72	5.06
Sc	21.6	17.7	11.9	27.3	28.7	23.6	34.0
Ti	13,580	11,490	5539	17,920	17,030	14,130	16,160
V	91	65	13	326	317	184	348
Cr	0	0	0	2	2	1	147
Co	12.6	7.6	4.2	28.7	28.1	20.7	36.4
Ni	0.3	0.3	0.3	3.9	4.0	2.0	55.2
Cu	12.3	9.4	7.4	39.2	35.8	25.2	88.3
Zn	150.3	157.5	118.4	121.3	118.8	123.3	100.8
Rb	34.9	43.8	56.0	16.7	19.0	24.7	15.5
Sr	399	263	133	267	258	236	360
Y	73.1	79.7	89.1	63.2	59.1	66.6	34.8
Zr	478	585	711	351	327	365	213
Nb	94.1	111.3	113.9	64.1	59.5	65.8	45.1
Cs	0.367	0.461	0.581	0.125	0.199	0.260	0.159
Ba	377	444	442	213	200	240	188
La	71.6	82.8	84.0	45.6	42.4	51.0	31.5
Ce	144.0	166.5	165.2	99.0	93.4	111.7	68.2
Pr	18.7	21.2	20.3	12.4	11.6	13.7	8.5
Nd	74.6	83.7	77.4	51.0	48.2	56.2	35.0
Sm	15.44	17.00	15.74	11.44	10.81	12.27	7.52
Eu	4.67	4.74	3.51	3.27	3.11	3.44	2.43
Gd	14.59	15.97	15.05	11.59	10.98	12.47	7.45
Tb	2.226	2.498	2.479	1.846	1.749	1.991	1.139
Dy	12.84	14.56	15.25	11.00	10.48	11.71	6.53
Ho	2.54	2.85	3.11	2.23	2.11	2.37	1.27
Er	6.87	7.87	9.01	6.20	5.86	6.61	3.45
Tm	0.981	1.141	1.366	0.901	0.861	0.967	0.486
Yb	6.10	7.18	8.89	5.70	5.45	6.08	3.03
Lu	0.893	1.067	1.340	0.844	0.809	0.900	0.440
Hf	11.09	14.43	18.00	8.79	8.24	9.33	5.06
Ta	6.002	6.540	6.800	4.024	3.575	4.063	2.795
Pb	3.36	4.15	4.49	2.06	2.04	2.69	1.57
Th	7.74	10.43	14.74	6.20	5.91	7.06	3.21
U	2.000	2.688	3.747	1.486	1.434	1.771	0.881
Isotopes							
^{87}Sr/^{86}Sr	0.703641	0.703635	0.703725	0.703529	0.703959	0.703758	0.703545
2SE	6.2	6.1	6.1	44.5	6	8.8	5.3
^{143}Nd/^{144}Nd	0.512890	0.512897	0.512909	0.512907	0.512933	0.512920	0.512906
2SE	5	6	5	6	5	5	6
^{206}Pb/^{204}Pb	19.08	19.09	19.11	19.09	19.09	19.11	19.29
^{207}Pb/^{204}Pb	15.591	15.590	15.594	15.598	15.598	15.597	15.603
^{208}Pb/^{204}Pb	39.09	39.10	39.08	39.07	39.06	39.08	39.23

	Stage 4	
Sample ID	D150	D153
Trace elements (ppm)		
Li	5.12	4.79
Sc	33.7	32.7
Ti	16,380	16,160
V	347	342
Cr	137	142
Co	36.3	35.2
Ni	55.3	53.1
Cu	88.3	82.3
Zn	99.5	99.9
Rb	15.4	15.9
Sr	369	366
Y	34.7	34.8
Zr	210	217
Nb	45.6	45.7
Cs	0.156	0.161

(*continued on next page*)

Table 2 (*continued*)

	Stage 4	
Sample ID	D150	D153
Ba	187	190
La	31.3	31.7
Ce	67.9	68.4
Pr	8.5	8.6
Nd	34.8	35.2
Sm	7.45	7.53
Eu	2.39	2.41
Gd	7.28	7.41
Tb	1.110	1.126
Dy	6.40	6.47
Ho	1.25	1.26
Er	3.37	3.40
Tm	0.474	0.484
Yb	2.95	2.99
Lu	0.430	0.441
Hf	4.88	5.07
Ta	2.808	2.767
Pb	1.57	1.78
Th	3.14	3.29
U	0.851	0.889
Isotopes		
$^{87}Sr/^{86}Sr$	0.703527	0.703541
2SE	10.5	5.9
$^{143}Nd/^{144}Nd$	0.512896	0.512915
2SE	6	6
$^{206}Pb/^{204}Pb$	19.29	19.28
$^{207}Pb/^{204}Pb$	15.603	15.604
$^{208}Pb/^{204}Pb$	39.23	39.23

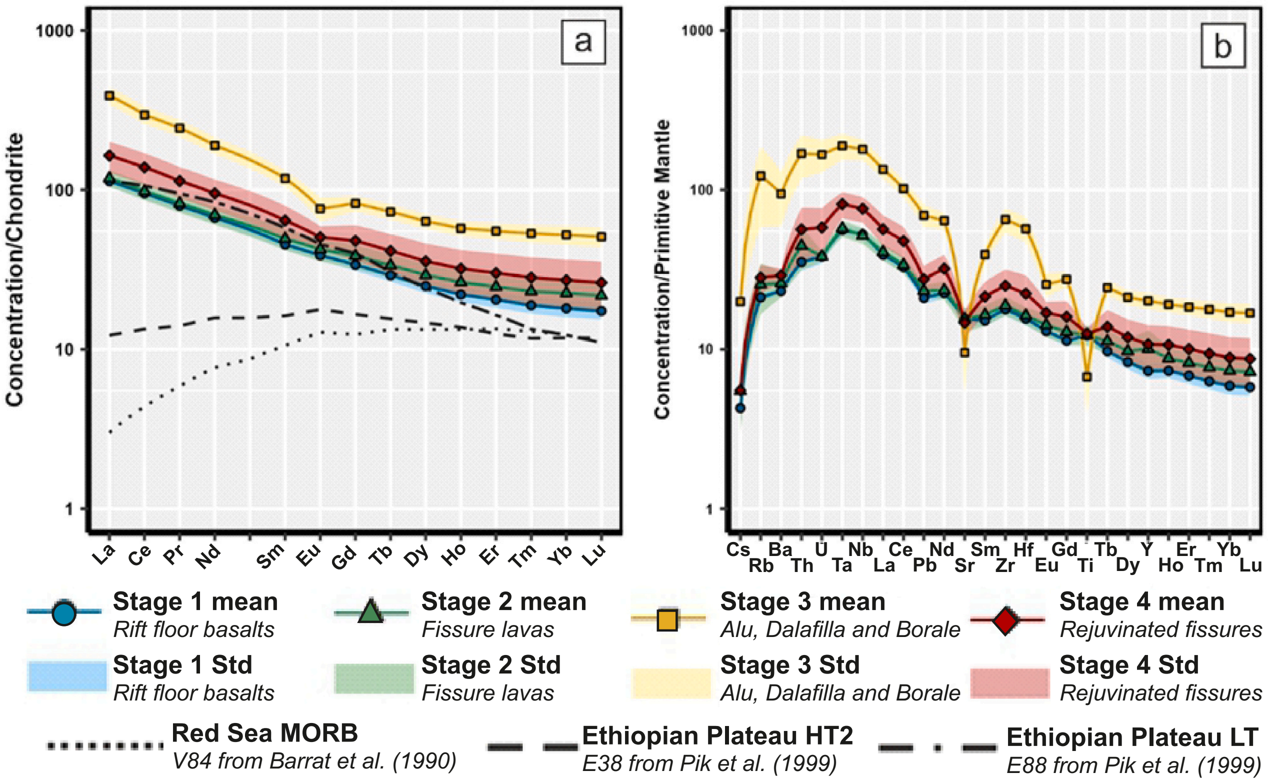

Fig. 4. Trace element characteristics of the EAVS volcanics. Samples have been separated using the relative chronology from Watts et al. (2020). The mean values of the stage are shown by the line and symbols, and the standard deviation about the mean of each stage is shown by the shaded region of the corresponding colour. Symbols are as in Fig. 2. Red Sea MORB profile (Barrat et al., 1990), LT and HT2 Ethiopian Plateau (Pik et al., 1999) profiles have been added for comparison. (a) REE plot, normalised using chondrite values from McDonough and Sun (1995). (b) Spider diagram using values for primitive mantle from Sun and McDonough (1989). (For interpretation of the references to colour in this figure legend, the reader is referred to the web version of this article.)

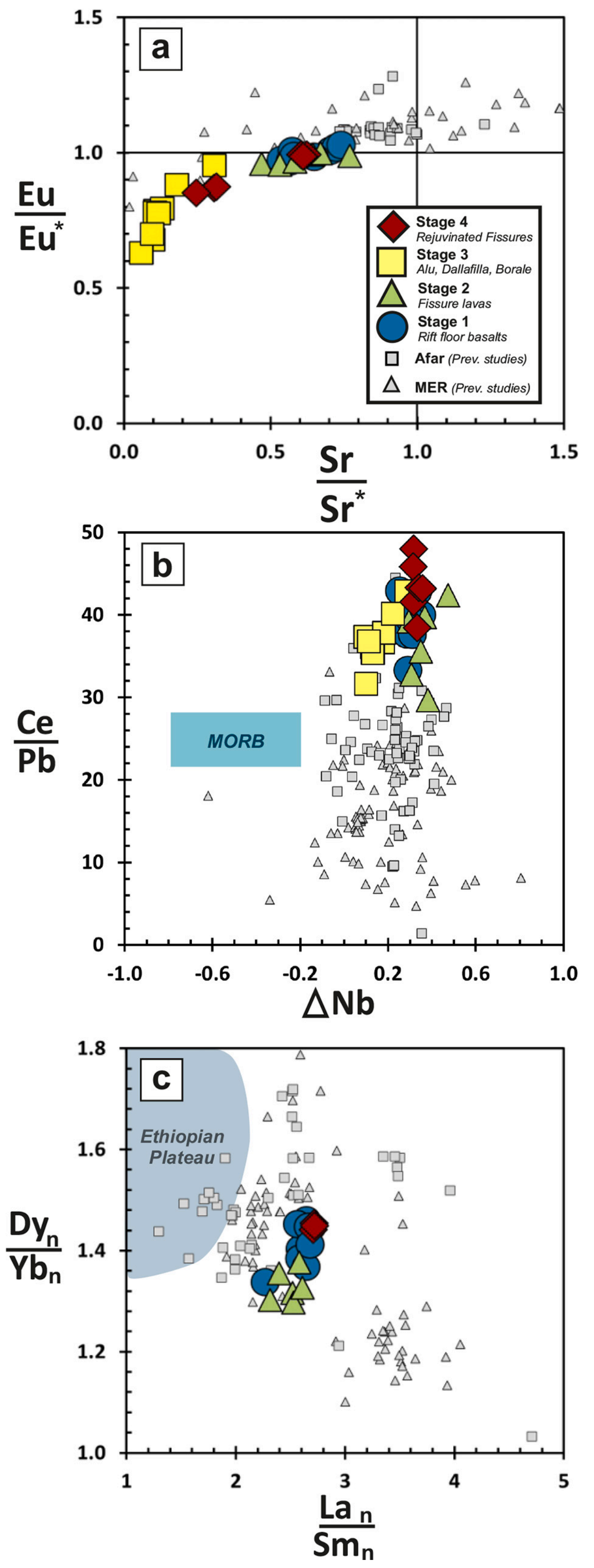

Fig. 5. Trace element plots. Symbols are as in Fig. 2. Top: Eu/Eu* (Eq.1) versus Sr/Sr* (Eq. 2). Middle: Ce/Pb versus ΔNb (Eq. 3). Bottom: Dy_n/Yb_n versus La_n/Sm_n both normalised to the primitive mantle (Sun and McDonough, 1989). Representative Afar and MER data are sourced from previously published data (references are provided in the caption to Fig. 3) and the Ethiopian Plateau field is sourced from Pik et al. (1999).

4.2. *Sr, Nd and Pb isotopes*

Sr, Nd and Pb isotopes of the Alu, Dalafilla and Borale lavas and pumice are presented in Table 2. All four stages exhibit $^{87}Sr/^{86}Sr$ in the range 0.7035–0.7040 (Fig. 6), with Stage 1 basalts showing the most restricted range (0.70352–0.70372) and Stage 4 the largest range (0.7035–0.7040). Stage 3 samples from Borale (Phase I; Watts et al., 2020) show minimal variation in $^{87}Sr/^{86}Sr$ (0.70363–0.70364). $^{143}Nd/^{144}Nd$ has a restricted range between 0.51288 and 0.51294 (Fig. 6), which is marginally greater than analytical reproducibility. Lead isotope ratios lie within a restricted range ($^{206}Pb/^{204}Pb$: 18.9–19.3; $^{207}Pb/^{204}Pb$: 15.588–15.603; $^{208}Pb/^{204}Pb$: 38.86–39.25, Fig. 6) relative to the published Afar and MER data ($^{206}Pb/^{204}Pb$: 17.6–19.9; $^{207}Pb/^{204}Pb$: 15.50–15.71; $^{208}Pb/^{204}Pb$: 37.90–40.10, Fig. 6) (Rooney, 2020b).

Co-variations of isotopes from Alu, Dalafilla, and Borale are shown alongside potential mantle and crustal components in Fig. 6. All EAVS lavas fall within the range of the Afar axial segments (Fig. 6), however EAVS lies close to the putative composition of the Afar Plume (Fig. 6) mantle end-member as defined by Rooney et al. (2012), but extend towards low $^{206}Pb/^{204}Pb$ components (EM1 and Arabian Nubian Shield crust; Davidson and Wilson, 1989; Teklay et al., 2010; Stracke et al., 2005). While the Alu, Dalafilla and Borale samples have similar Pb-isotope compositions to EM2 (Fig. 6a-d), their Sr—Nd isotope compositions lie off the EM2 field (Fig. 6e-f).

No progressive changes in Sr-Nd-Pb isotopes are observed throughout the evolution of Alu, Dalafilla and Borale, nor can we detect any appreciable difference in isotopic values between these edifices, apart from that observed for $^{87}Sr/^{86}Sr$ within Stage 3 (Fig. 6).

5. Discussion

5.1. *Magma generation*

The Alu, Dalafilla and Borale basalts are characterised by Dy_n/Yb_n: 1.09–1.46 (Fig. 5c). These characteristics indicate that the mantle source of the EAVS volcanics is dominated by spinel rather than garnet facies melting, similar to that observed in the Central Afar Gulf volcanics (1.1–0.6 Ma; Tortelli et al., 2022). The depth of the garnet lherzolite and spinel lherzolite transition globally is debated, with estimates ranging from 40 to 100 km (Su et al., 2010). Previous geochemical modelling studies across the Afar region have estimated the garnet-spinel transition to lie in the higher end of those estimates, between 70 and 100 km (Ayalew et al., 2018; Ferguson et al., 2013). When compared to the 30-million-year-old Ethiopian Plateau (Dy_n/Yb_n: 1.35–2.4, Fig. 5c; Pik et al., 1999), the values indicate that EAVS melt contains a higher proportion of spinel lherzolite, implying that the melting depth may have shallowed over the evolution of the rift (i.e., 30 Myr).

To estimate the melt fraction and relative proportions of mantle components, we performed melt modelling for each of the basaltic samples (Stages 1, 2, and 4; Table 1, Fig. 2) using the magmatic petrology program, PetroGram, which produces forward and inverse geochemical models for melting processes (Gündüz and Asan, 2021). Only basaltic samples with an MgO $>$ 5.5 wt% were considered for the melt modelling to minimise the effects of fractionation. All sample data were best replicated using dynamic melting models (both modal and non-modal) with 0–15% garnet lherzolite and 85–100% spinel lherzolite (Fig. 7). Stage 1 basalts are likely to have formed from a source containing 10–15% garnet lherzolite, with an overall melt fraction of 3.5–4.5%. Stage 4 was similar to Stage 1, comprising 15% garnet lherzolite and 85% spinel lherzolite in the source, with 3–4.5% melting (Fig. 7). Modelling of Stage 2 samples indicates that they were formed from 0 to 10% garnet lherzolite and 90–100% spinel lherzolite, with 4.5–5.5% melting (Fig. 7).

To investigate this further, we used the major element compositions of the basalts (Watts et al., 2020) to estimate the pressures and

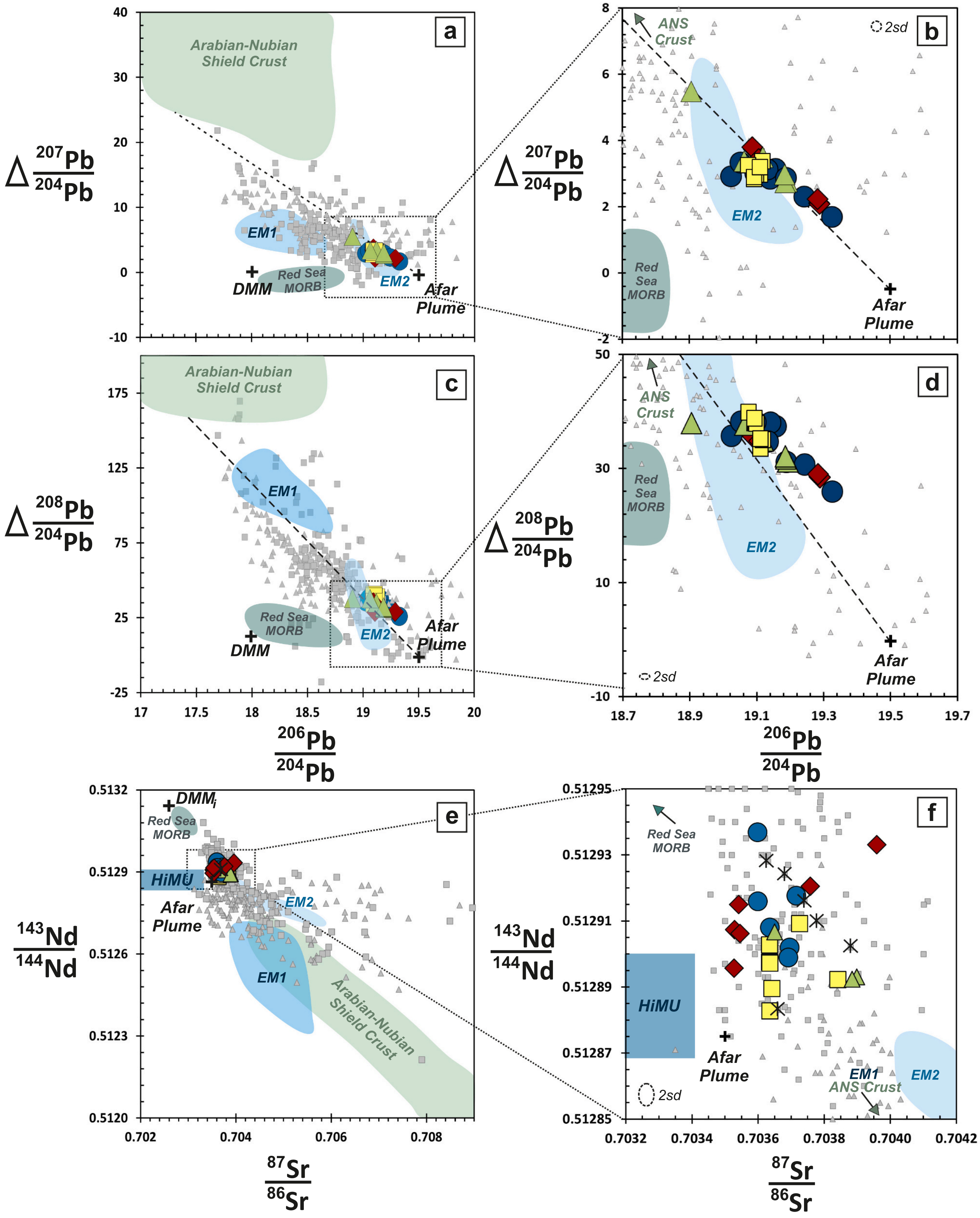

Fig. 6. (a) and (b) $\Delta^{207}Pb/^{204}Pb$ versus $^{206}Pb/^{204}Pb$; (c) and (d) $\Delta^{208}Pb/^{204}Pb$ versus $^{206}Pb/^{204}Pb$; (e) and (f) $^{143}Nd/^{144}Nd$ versus $^{87}Sr/^{86}Sr$. $\Delta^{207}Pb/^{204}Pb$ and $\Delta^{208}Pb/^{204}Pb$ represents the vertical deviation in $^{207}Pb/^{204}Pb$ or $^{208}Pb/^{204}Pb$ (respectively) from the northern hemisphere reference line (NHRL) and is calculated by: (1) $\Delta^{207}Pb/^{204}Pb = 100[(^{207}Pb/^{204}Pb) - (0.1084(^{206}Pb/^{204}Pb) - 13.491)]$ and (2) $\Delta^{208}Pb/^{204}Pb = 100[(^{208}Pb/^{204}Pb) - (1.209(^{206}Pb/^{204}Pb) - 15.627)]$ (Hart, 1984). All plots highlight the mantle end members and potential contaminants associated with the basalts from the EAVS. (b, d, f) represent zoomed-in versions of (a, c, e) respectively. Mantle end members are shown as follows: Afar Plume (shown as black cross, Rooney et al., 2012), Depleted MORB Mantle (DMM, shown as black cross; Stracke et al., 2005), EM1 & EM2 (Jackson and Dasgupta, 2008); Arabian Nubian Shield Crust (Davidson and Wilson, 1989; Teklay et al., 2010); Red Sea MORB (Barrat et al., 1990; Volker et al., 1993), HIMU (Woodhead, 1996). Symbols are as in Fig. 2. The dashed lines on (a-d) represent the mixing trajectory of the Afar plume with the crustal field (from Davidson and Wilson, 1989). Black stars show previously published data for Alu, Dalafilla and Borale (Barrat et al., 1998).

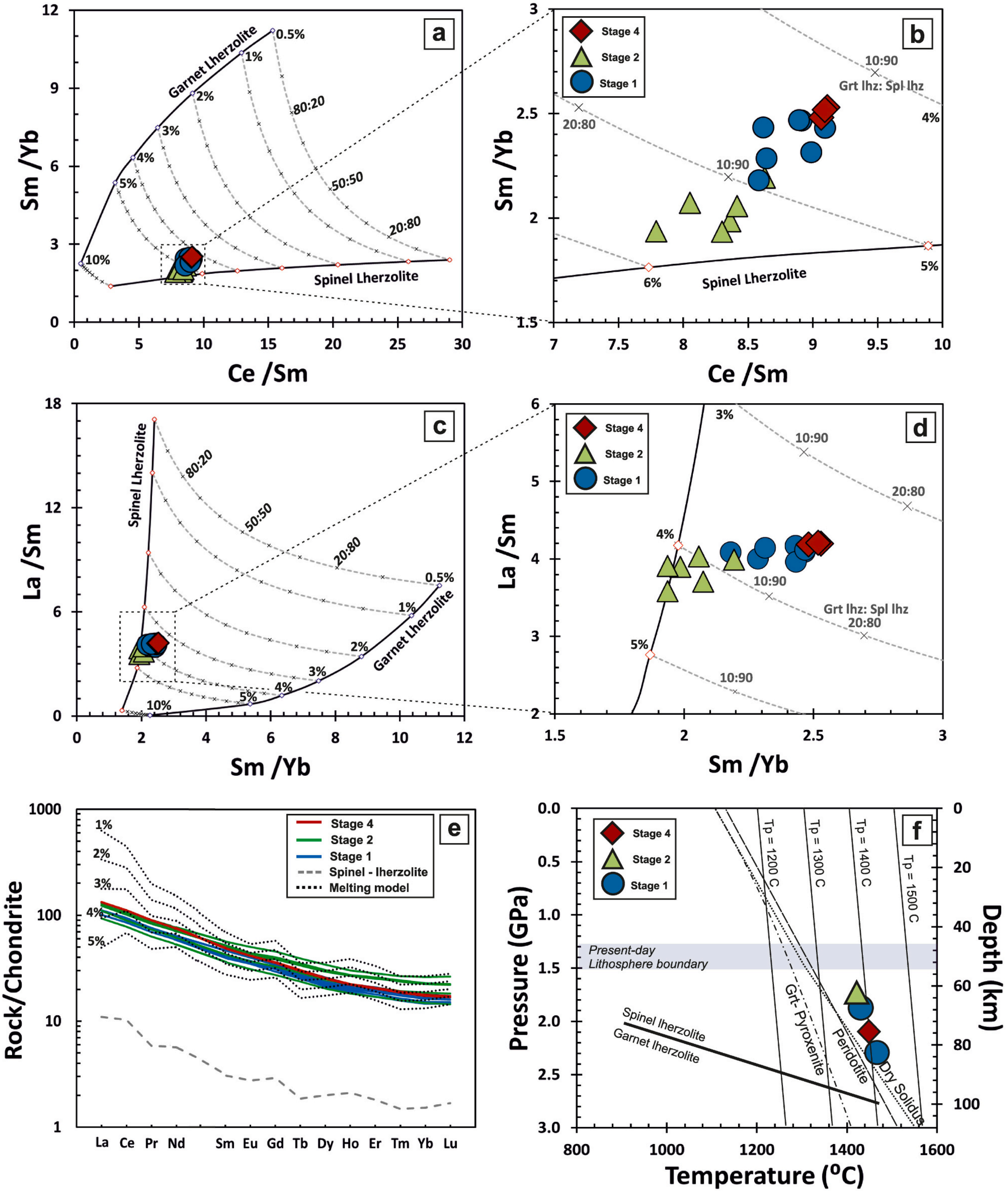

Fig. 7. Depth of melting: (a-e) Results from the trace element modelling (Gündüz and Asan, 2021) of dynamic melting of a spinel lherzolite (McDonough 1990) and garnet lherzolite (Frey 1980) source. Samples were normalised to chondrite values (Sun and McDonough, 1989). (f) Pressure-temperature diagram of the basaltic samples using the model of Lee et al. (2009); other modelled lines are from Ayalew et al. (2018). Uncertainties in the pressure and temperature estimates are smaller than the symbol size (<0.3 GPa and < 40 °C). Lithospheric thickness estimates shown are from Bastow et al. (2011). Only samples fulfilling the conditions stated within Lee et al. (2009) and with an MgO > 5.5 wt% were considered, as they were the most primitive samples within the study. Symbols are as in Fig. 3.

Table 3

Si—Mg thermobarometry results using the method of Lee et al. (2009). Only the most primitive samples (MgO >5.5 wt%) that fit the conditions laid out by Lee et al. (2009) were considered. Prior to using the method of Lee et al. (2009), back-correcting for olivine-clinopyroxene-plagioclase fractionation was done using the Petrolog v.3.1.1.3 model (Danyushevsky and Plechov, 2011) following the methodology of Chiasera et al. (2021). For further details see supplementary document S2. To calculate the depth we used the equation of $P = \rho g h$ re-arranged to $h = \frac{P}{\rho g}$, where g is acceleration due to gravity, and h is height. The crustal density (ρ) value (basaltic flows and related spatter) of ~2850 kg m^{-3} from Mahatsente et al. (1999) was assumed.

Sample	Stage	MgO (wt %)	Temperature (°C)	Pressure (GPa)	Depth (km)
G65	1	7.15	1431	1.89	67.8
M7	1	6.00	1471	2.31	82.9
F49	2	6.57	1420	1.77	63.5
D153	4	5.58	1451	2.10	75.2

temperatures of equilibration with the mantle (see Table 3 and Supplementary Document S2), employing the Si—Mg thermobarometer of Lee et al. (2009). The model of Lee et al. (2009) only corrects for olivine fractionation so, prior to the use of the thermobarometer, basalt compositions were corrected to primary melt composition (for olivine, clinopyroxene and plagioclase fractionation) using the Petrolog v.3.1.1.3 model (Danyushevsky and Plechov, 2011) following the methodology of Chiasera et al. (2021; see Supplementary Document S2 for more details). The fO_2 values (NNO-4) for the reverse-crystallisation were taken from Watts et al. (2020).

After correction to primary melt compositions, the Si—Mg thermobarometer calculations returned potential temperature estimates ranging from 1420 to 1471 °C at approximately 1.77–2.31 ± 0.2 GPa (Fig. 7). These estimates, intended to be used as guidelines, correspond to depths ranging from 64 to 83 km (Fig. 7f), which are similar to, but slightly deeper than, the lithospheric thickness estimates from both active and passive source seismic imaging across the region (Fig. 7f) (Bastow et al., 2011; Lavayssiere et al., 2018). Similar temperature and depth conditions have also been inferred previously within the Afar region by Ferguson et al. (2013), who used the Si—Mg thermobarometer to suggest the last melt-mantle equilibria depth beneath the on-axis DVS (central Afar) occurred at 2.3–2.6 GPa and 1472–1489 °C. Ayalew et al. (2018) obtained equilibrium depths for the flood basalts (31–29 Ma; Hofmann et al., 1997) ranging from approximately 50–65 km and temperatures of 1350–1425 °C. This further indicates that the temperature of the last melt-mantle equilibria has remained consistent during the rifting within Afar, but the depth of equilibria varies across the Afar triangle even in 'modern' (< 1 Ma) times. Given the stark differences in crustal thickness between DVS (22 km) and the EAVS (15 km), we propose that the substantial (~33% difference) northward increase in plate thinning into the Danakil Depression and resultant shallowing of the top of the melt zone beneath the plate (Hammond et al., 2011; Lewi et al., 2016) could explain the inferred shallowing of melt-mantle equilibria.

Combining melt modelling (using trace element ratios) with temperature and pressure estimates, we find that Stages 1 and 4 have experienced similar melt generation histories. The most recent (i.e., Stage 4) mantle equilibrium depth is estimated to be 75 km, with a maximum garnet:spinel lherzolite ratio of 85:15. To generate a melt with a source consisting of 15% garnet lherzolite, melting onset must have occurred significantly deeper than the garnet-spinel transition zone.

Samples from Stage 2 show a decrease in the proportion of garnet lherzolite in the melt source (<10%; Fig. 7). This likely indicates a shallower depth of melting than all other stages of EAVS evolution, but the onset of melting must still occur at depths of >70 km (Ayalew et al., 2018; Ferguson et al., 2013) to satisfy the incorporation of garnet lherzolite. The overall shallower melting, supported by pressure estimates within this study, is accompanied by a higher degree of melting (4.5 to 5.5%; Fig. 7). This could be a result of changes in the Afar area including: (1) hotter mantle (Ferguson et al., 2013) and (2) an increase in the rate of plate thinning and concomitant increase in decompression melting (Niu, 2021). (1) is ruled out as the temperature estimates were broadly consistent across all four stages. For (2) an increased rate of plate thinning would likely be associated with an increase in the height of the melting column producing a higher melt fraction. While (2) may offer a potential explanation, a current lack of absolute dates for the samples means that any correlation between melt fraction and variation in thinning rates is not currently possible.

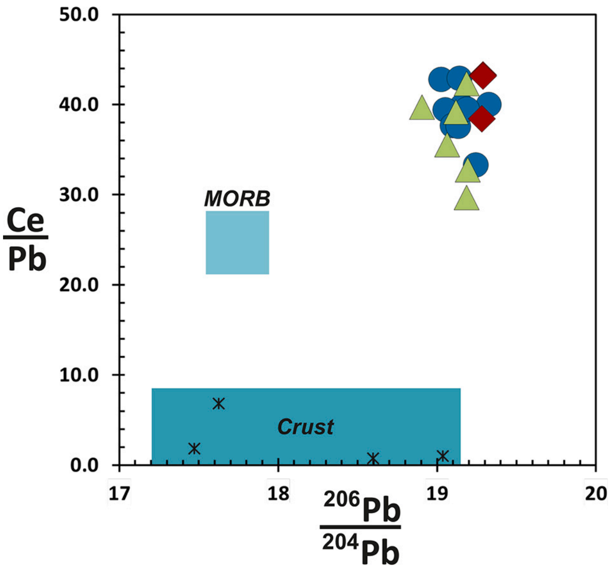

Fig. 8. Ce/Pb versus $^{206}Pb/^{204}Pb$. End members shown are the typical values of MORB (Hofmann et al., 1986) and approximate crust (as defined by the values of Davidson and Wilson (1989) shown as black stars). Sample symbols are as in Fig. 3.

Overall, the samples within this study, when combined with previous studies of Afar and the MER (Armitage et al., 2015; Ayalew et al., 2018; Chiasera et al., 2021; Ferguson et al., 2013), indicate that the temperature of the mantle melts within the region have remained relatively consistent throughout time (~1400–1490 °C). No clear link between stage of rifting and melt fraction is apparent during the rifting history of Afar, an observation consistent with the comparable melt fractions (~3–4%) in the MER (Feyissa et al., 2017) and Tanzania (Mana et al., 2012), where rifting is at a relatively early stage. However, melt abundance and depth of melting appears to vary between volcanic segments in Afar (e.g., EAVS and DVS) as well as varying throughout the evolution of individual volcanic segments. We propose this is a result of a varying rate of plate thinning over time and across Afar, leading to changes in the rate of decompression and subsequent melting conditions (Niu, 2021).

5.2. Mantle source characteristics

Trace element ratios (e.g., Ce/Pb, ΔNb, and Zr/Hf) can provide insights into the asthenospheric and lithospheric components involved in the production and transport of Afar magmas. The ΔNb parameter has previously been used to distinguish a plume signature (ΔNb > 0) from a depleted mantle MORB (DMM) signature (ΔNb < 0) within Icelandic lavas (Fitton et al., 1997). ΔNb is insensitive to crustal contamination or the extent of melting, and a positive ΔNb is taken to reflect a mantle plume source melting at depth (Fitton et al., 1997). All samples analysed from Alu, Dalafilla and Borale exhibit a positive ΔNb (0.09–0.47; Fig. 5), consistent with the hypothesis that a plume beneath the region

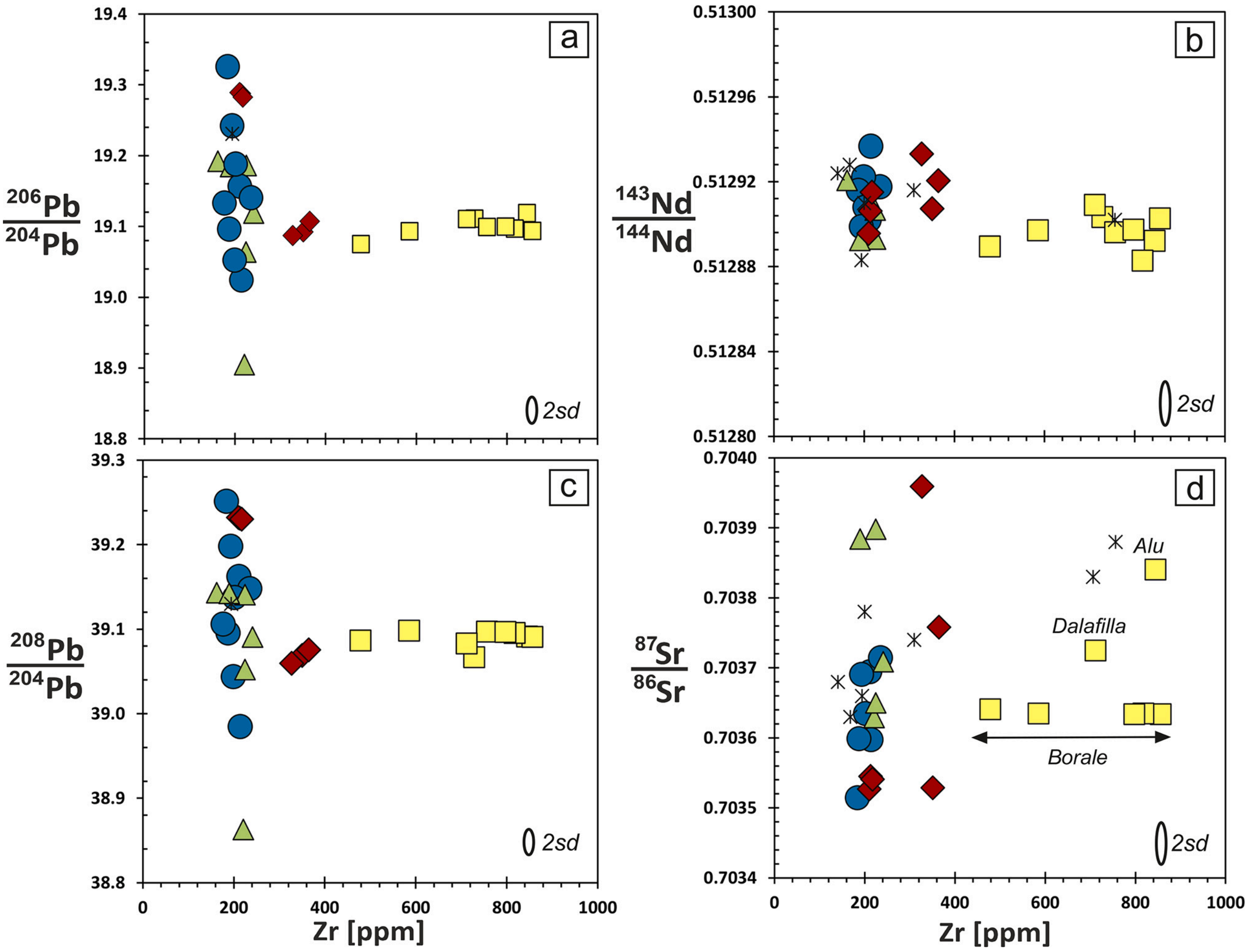

Fig. 9. Zirconium concentration versus radiogenic isotopes: (a) $^{206}Pb/^{204}Pb$, (b) $^{143}Nd/^{144}Nd$, (c) $^{208}Pb/^{204}Pb$, (d) $^{87}Sr/^{86}Sr$. 2 standard deviations (2sd) is equivalent to the size of the symbol. Symbols are as in Fig. 3. Black stars show previously published data for Alu, Dalafilla and Borale (Barrat et al., 1998).

contributes the dominant component during melting (Rooney et al., 2012; Rooney et al., 2020c).

Compared to other studies across Afar (Ayalew et al., 2018; Barrat et al., 1998; Hutchison et al., 2018; Rooney, 2020b, 2020c), the Ce/Pb ratio for the Alu, Dalafilla, and Borale samples are high, ranging from 29.7 to 48.0 (Figs. 5 & 8). Samples with Ce/Pb > 30 are commonly attributed to a recycled mantle source that has been depleted in fluid mobile elements (i.e., Pb, Ba, Sr, K) during subduction, therefore resulting in high fluid-immobile-element to fluid-mobile-element ratios (i.e., Ce/Pb; Hofmann et al., 1986). High Ce/Pb ratios, combined with the ΔNb values, of our samples supports the idea that a recycled subducted ocean lithosphere, commonly entrained within mantle plumes (Hofmann and White, 1982), is present in the mantle source.

However, the Ce/Pb variation across the samples (Figs. 5 & 8), irrespective of SiO_2 content, indicates the potential for contamination of primary mantle-derived magmas. With respect to Ce/Pb, depleted asthenospheric (MORB-like) mantle is commonly reported as 25 ± 5 and the continental crust typically has values of ~4 (Hofmann et al., 1986), both of which could lower the Ce/Pb if their melts were mixed with melts of high Ce/Pb (with Ce/Pb as high as 48 in sample CH23). Such mixing could account for the range in Ce/Pb, but this ratio alone cannot differentiate between potential contaminants.

Using radiogenic isotope compositions, we can gain further insights into the specific mantle and crustal components involved in the system. Alu, Dalafilla and Borale volcanics (Fig. 6) can be explained by contributions from two or three distinct domains—that is, the Afar plume, EM1 and/or Arabian Nubian Shield crust—with the Afar plume dominating and the crust or EM1 likely being a key contaminant (Fig. 6). Whilst a mixing trend between the Afar plume and Arabian Nubian Shield crust domains provides an approximate match to the Alu, Dalafilla and Borale compositions (Fig. 6a-d), it is not exact and therefore may necessitate minor EM1 involvement.

Previously published $\delta^{18}O$ data from the Alu, Dalafilla and Borale volcanoes range from 5.40 ± 0.09 to 6.42 ± 0.01 ‰ (Barrat et al., 1998), which is firmly within the range previously observed for typical mantle derived basalts (5.2–5.8‰; Eiler, 2001) or samples which have subsequently experienced fractional crystallisation, which can increase the $\delta^{18}O$ value by up to 0.6 ‰ (Hutchison et al., 2018). When the $\delta^{18}O$ values are combined with observed values of Ta/Th (0.61–0.78), $^{87}Sr/^{86}Sr$ (0.7036–0.7038), and ε_{Nd} (4.91–5.04) from within the EAVS, we can infer a strong influence of a mantle plume member without any significant contamination from assimilating hydrothermally altered crust (Barrat et al., 1998; Hutchison et al., 2018).

Upon further investigation using a combination of Ce/Pb alongside $^{206}Pb/^{204}Pb$ (Fig. 8), the lavas appear scattered about a general trend towards the crustal values from the Arabian Nubian Shield (Davidson and Wilson, 1989). While there is some scatter, the lavas have a Ce/Pb >29 indicating a dominantly mantle signature and hence the overall influence of crustal assimilation is likely limited. The slight scatter of the samples in isotopic space (Fig. 8 & Fig. 9), could be a result of either minor assimilation of crust or EM1 (of varying composition) or a result of a chemically heterogeneous Afar plume. Given the observed high Ce/Pb, the Afar plume is likely linked to the recycling of a previously subducted oceanic lithosphere (Hofmann et al., 1986), which can

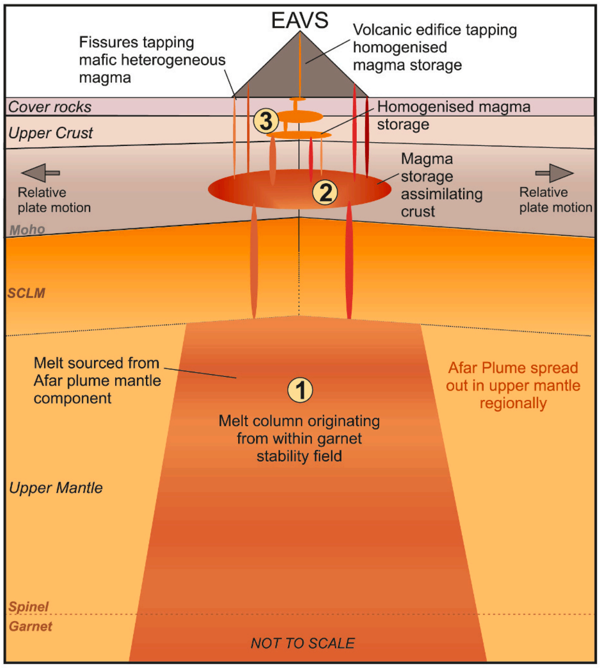

Fig. 10. Schematic diagram showing the generation of the volcanic rocks within the EAVS. (1) shows the generation of the melt with an Afar plume signature (see section 4.1). (2) shows the assimilation of the lower crust, resulting in the EAVS magmas obtaining a variable degree of lower crustal radiogenic isotope ratio signatures (see section 4.2). (3) shows the isotopic homogenisation of the EAVS magmas during fractional crystallisation and compositional evolution in high-level storage zones.

potentially introduce heterogeneities within the source. Further investigation of the underlying crust in Afar is required to fully address this outstanding question.

5.3. Magma pathway through the plumbing system

Radiogenic isotope ratios demonstrate the heterogeneity within the Alu, Dalafilla and Borale basalts (Tables 1-2, Figs. 6, 8, 9). The cause of these heterogeneities could be: (1) a heterogeneous mantle plume source such as those observed within Hawaii (Abouchami et al., 2005), Samoa (Jackson et al., 2014), and the Canary Islands (Taylor et al., 2020), giving rise to range of starting compositions; (2) varying amounts of assimilation of a crustal and/or an EM1 component, which would systematically reduce the $^{206}Pb/^{204}Pb$ value with increasing contamination; (3) a combination of both a heterogeneous plume source and varying amounts of contamination by the crust and/or an EM1 component. Based on the observed isotopic characteristics (Fig. 6), the basalts all underwent assimilation of the crust but to varying degrees.

The more evolved samples of Stages 3 and 4 have a narrow range in $^{206}Pb/^{204}Pb$ (19.0751 and 19.1189, Fig. 9). This isotopic consistency in evolved Stages 3 and 4 is also reflected in the $^{208}Pb/^{204}Pb$ and $^{143}Nd/^{144}Nd$ (Fig. 9). Stages 3 and 4 (again targeting samples with Zr >300 ppm) have $^{87}Sr/^{86}Sr$ in the range 0.7035–0.70395 (± 0.00003), displaying variability between the volcanic centres not shown by the other isotope ratios. The highest values are from Alu (CH20) and Dalafilla (D59), with Borale samples remaining consistently low at around 0.70363. The two outliers found at Alu and Dalafilla with slightly higher $^{87}Sr/^{86}Sr$ (CH20 and F59 respectively, Fig. 9d) are likely a result of increased alteration by hydrothermal fluids with a higher $^{87}Sr/^{86}Sr$, especially given their low Sr concentration and similar $^{206}Pb/^{204}Pb$ and $^{143}Nd/^{144}Nd$ to the other samples. The deviation towards a higher $^{87}Sr/^{86}Sr$ is most prominent in the northernmost sample (CH20, Alu, Fig. 9d), indicating this alteration might be linked to the hydrothermal activity at Dallol volcano situated north of the segment (Cavalazzi et al., 2019).

In addition, $^{206}Pb/^{204}Pb$ values of evolved samples (Table 2) fall approximately at the median (19.1) of the $^{206}Pb/^{204}Pb$ values for the basaltic samples (Fig. 9), similar to that observed for the other isotope ratios ($^{207}Pb/^{204}Pb$, $^{208}Pb/^{204}Pb$, $^{87}Sr/^{86}Sr$, and $^{143}Nd/^{144}Nd$). Given this observation, combined with the zoned plagioclases reported in Watts et al. (2020), we believe that repeated basaltic additions to an upper crustal storage system, averaging the isotopic range observed, is most likely.

The broadly consistent $^{206}Pb/^{204}Pb$, $^{207}Pb/^{204}Pb$, $^{208}Pb/^{204}Pb$, and $^{143}Nd/^{144}Nd$ values observed within the more evolved samples also indicates that minor, if not negligible, upper crustal contamination occurred during melt mixing and magma differentiation. The consistency of isotopic compositions of evolved samples across all three volcanoes suggests their magma storage and plumbing systems could be partially interconnected, with magmas erupting at any of the volcanic centres (Alu, Dalafilla or Borale). This is consistent with the findings of Pagli et al. (2012), who using results from InSAR and Mogi modelling, modelled a 10-km-long elongated shallow axial magmatic system linking multiple centres (the Alu dome and Dalafilla in this case), which fed the 2008 fissural eruption between the two centres. Similar observations have been observed at segments (i.e. Boset Bericha, Kone and Fantale) within the MER (Siegburg et al., 2023).

Previous studies (Illsley-Kemp et al., 2018; Pagli et al., 2012) have identified possible sites of magma storage at depths of 1, 4 and 12 km. We find no clear relationship between magma evolution (i.e., as shown by Zr content) and the presence of a crustal signature (Fig. 6). Given this, alongside the minimal isotopic variation shown amongst the more evolved samples (Fig. 9), we suggest that most of the differentiation occurs within the upper magmatic storage systems (1 and/or 4 km), with various levels of lower crustal contamination. Variable levels of lower crustal contamination in the basaltic samples indicates the presence of a deeper storage system (at ~12 km depth) which may have been bypassed by the ascending basaltic magmas. Hammond et al. (2011) has estimated that the upper crust begins at ~8 km at the EAVS. Therefore, we find it most likely that magmas assimilate the lower crust while the magma differentiation dominantly occurs in the upper crust (Fig. 10).

Multi-level storage is a commonly observed phenomenon within rifts of different maturity levels including examples such as Kraftla in Iceland (Wright et al., 2012), the MER, and mid ocean ridges (Illsley-Kemp et al., 2018). Within this study of a proto-oceanic rift, we find evidence for a multi-level storage system, including a shallow crustal sill systems (at ~1–4 km depth). This is similar to that observed at fast spreading ridges where the high magma supply rate is thought to sustain long lived axial sills in the uppermost crust (Phipps Morgan and Chen, 1993).

6. Conclusions

We generated new trace element and Sr-Nd-Pb isotope data for major volcanic groups of the Alu, Dalafilla and Borale Volcanoes of Afar, and report the following findings:

- Sr-Nd-Pb isotopes within the basalts are heterogeneous, which may be explained by contamination from an EM1 mantle component and/or the Afar plume mantle source having a heterogeneous isotopic signature.
- The main mantle components are primarily the Afar plume (C-like) component, with varying amounts of contamination from the crust and/or EM1 (Fig. 10).
- Dynamic melting modelling shows that the oldest basalts (Stage 1) formed from a source containing 10–15% garnet lherzolite and 85–90% spinel lherzolite. The volcanoes then underwent a period of shallower melting (Stage 2) where the source contained 0–10% garnet lherzolite and 90–100% spinel lherzolite. Following this, the melting level became progressively deeper, resulting in the most

recent basalts (Stage 4) being sourced from 15% garnet lherzolite and 85% spinel lherzolite (Fig. 10).

- The degree of melting (~4%) has been reasonably continuous across all three volcanoes, except for one period early in the evolution of Alu and Dalafilla (Stage 2) where a higher degree of melting (up to 5.5%) is inferred.
- The melt-mantle equilibrium depth at the EAVS is sometimes shallower (64 to 83 km) than that observed elsewhere in the Afar region (i.e., >75 km at the DVS; Fergusson et al., 2013), which is potentially a result of the substantial thinning of the crust beneath the EAVS.
- Isotopic homogeneity of evolved lavas from all three volcanoes (Alu, Dalafilla and Borale) indicates they tap the same storage system which integrated the isotopic diversity present in the basaltic input (Fig. 10).
- We propose that magma differentiation largely occurs when the melt resides at depths of approximately 1–4 km (Fig. 10).
- We attribute variations of melt abundance and melting depth across the evolution of the volcano to a varying rate of crustal thinning, thereby changing the conditions of decompression melting.
- We find evidence for multi-level magma storage at the EAVS including shallow crustal sill systems (1–4 km) which is similar to that observed at fast spreading ridges.

Declaration of Competing Interest

Emma J. Watts reports financial support was provided by Geologists' Association. Emma J. Watts reports financial support was provided by National Environmental Research Council. Thomas M. Gernon reports financial support was provided by National Environmental Research Council. Derek Keir reports financial support was provided by Government of Italy Ministry of Education University and Research. Carolina Pagli reports financial support was provided by Government of Italy Ministry of Education University and Research.

Acknowledgements

This research was funded by the Natural Environmental Research Council [grant number NE/L002531/1]. E.J.W was supported by the Wyley Fund of the Geologists' Association. T.M.G was supported by a Natural Environmental Research Council grant [NE/R004978/1]. D.K. and C.P., are funded by 2017 PRIN project - protocol MIUR: 2017P9AT72 PE10. We acknowledge the use of rocks from the Afar Repository of the University of Pisa, Italy (http://repositories.dst.unipi.it/index.php/home-afar). We acknowledge all those involved in the field-campaign in the 1960s. We thank Laura De Dosso for her help with the Afar Repository samples. We thank Matthew Cooper, Agnes Michalik and Andy Milton for their help and expert guidance with the laboratory work. We thank Gianmaria Tortelli for his discussions about volcanism within the region. We also thank the editor Dr. Greg Shellnutt as well as Dr. Karine Carvas and an anonymous reviewer for their constructive comments on the manuscript.

Appendix A. Supplementary data

Supplementary data to this article can be found online at https://doi.org/10.1016/j.lithos.2023.107311.

References

Abouchami, W., Hofmann, A.W., Galer, S.J.G., Frey, F.A., Eisele, J., Feigenson, M., 2005. Lead isotopes reveal bilateral asymmetry and vertical continuity in the Hawaiian mantle plume. Nature 434 (7035), 851–856. https://doi.org/10.1038/nature03402.

Armitage, J.J., Ferguson, D.J., Goes, S., Hammond, J.O.S., Calais, E., Rychert, C.A., Harmon, N., 2015. Upper mantle temperature and the onset of extension and break-up in Afar, Africa. Earth Planet. Sci. Lett. 418, 78–90. https://doi.org/10.1016/j.epsl.2015.02.039.

Ayalew, D., Jung, S., Romer, R.L., Garbe-Schönberg, D., 2018. Trace element systematics and Nd, Sr and Pb isotopes of Pliocene flood basalt magmas (Ethiopian rift): a case for Afar plume-lithosphere interaction. Chem. Geol. 493, 172–188. https://doi.org/10.1016/j.chemgeo.2018.05.037.

Barberi, F., Varet, J., 1970. The Erta Ale volcanic range (Danakil Depression, Northern Afar, Ethiopia). Bull. Volcanol. 34, 848–917. https://doi.org/10.1007/BF02596805.

Barrat, J.A., Jahn, B.M., Joron, J.L., Auvray, B., Hamdi, H., 1990. Mantle heterogeneity in northeastern Africa: evidence from Nd isotopic compositions and hygromagmaphile element geochemistry of basaltic rocks from the Gulf of Tadjoura and southern Red Sea regions. Earth Planet. Sci. Lett. 101, 233–247.

Barrat, J.A., Fourcade, S., Jahn, B.M., Cheminée, J.L., Capdevila, R., 1998. Isotope (Sr, Nd, Pb, O) and trace-element geochemistry of volcanics from the Erta'Ale range (Ethiopia). J. Volcanol. Geotherm. Res. 80 (1–2), 85–100. https://doi.org/10.1016/S0377-0273(97)00016-4.

Bastow, I.D., Keir, D., 2011. The protracted development of the continent–ocean transition in Afar. Nat. Geosci. 4 (4), 248–250. https://doi.org/10.1038/ngeo1095.

Bastow, I.D., Keir, D., Daly, E., 2011. Project EAGLE: probing the transition from continental rifting to incipient sea floor spreading in Ethiopia. Geol. Soc. Am. Spec. Pap. 478, 51–76. https://doi.org/10.1130/2011.2478(04).

Cavalazzi, B., Barbieri, R., Gómez, F., Capaccioni, B., Olsson-Francis, K., Pondrelli, M., et al., 2019. The Dallol geothermal area, Northern Afar (Ethiopia)—an exceptional planetary field analog on Earth. Astrobiology 19 (4), 553–578. https://doi.org/10.1089/ast.2018.1926.

Chambers, E.L., Harmon, N., Keir, D., Rychert, C.A., 2019. Using Ambient Noise to image the Northern East African Rift. Geochem. Geophys. Geosyst. 20 (4), 2091–2109. https://doi.org/10.1029/2018gc008129.

Chiasera, B., Rooney, T.O., Girard, G., Yirgu, G., Grosfils, E., Ayalew, D., Mohr, P., Zimbelman, J.R., Ramsey, M.S., 2018. Magmatically assisted off-rift extension—the case for broadly distributed strain accommodation. Geosphere 14 (4), 1544–1563. https://doi.org/10.1130/ges01615.1.

Chiasera, B., Rooney, T.O., Bastow, I.D., Yirgu, G., Grosfils, E.B., Ayalew, D., Mohr, P., Zimbelman, J., Ramsey, M., 2021. Magmatic rifting in the Main Ethiopian Rift began in thick continental lithosphere; the case of the Galema Range. Lithos 406-407. https://doi.org/10.1016/j.lithos.2021.106494.

Danyushevsky, L.V., Plechov, P., 2011. Petrolog3: Integrated software for modeling crystallization processes. Geochem. Geophys. Geosyst. 12 (7), n/a–n/a. https://doi.org/10.1029/2011gc003516.

Davidson, J.P., Wilson, I.R., 1989. Evolution of an alkali basalt-trachyte suite from Jebel Marra volcano, Sudan, through assimilation and fractional crystallization. Earth Planet. Sci. Lett. 95, 141–160. https://doi.org/10.1016/0012-821X(89)90173-8.

DIGIS Team, 2021. GEOROC Compilation: Rift. https://doi.org/10.25625/KAIVCT (Accessed 20th June 2022).

Ebinger, C.J., Keir, D., Ayele, A., Calais, E., Wright, T.J., Belachew, M., Hammond, J.O.S., Campbell, E., Buck, W.R., 2008. Capturing magma intrusion and faulting processes during continental rupture: seismicity of the Dabbahu (Afar) rift. Geophys. J. Int. 174 (3), 1138–1152. https://doi.org/10.1111/j.1365-246X.2008.03877.x.

Eiler, J.M., 2001. Oxygen isotope variations of basaltic lavas and upper mantle rocks. Rev. Mineral. Geochem. 43 (1), 319–364. https://doi.org/10.2138/gsrmg.43.1.319.

Ferguson, D.J., Maclennan, J., Bastow, I.D., Pyle, D.M., Jones, S.M., Keir, D., Blundy, J. D., Plank, T., Yirgu, G., 2013. Melting during late-stage rifting in Afar is hot and deep. Nature 499 (7456), 70–73. https://doi.org/10.1038/nature12292.

Feyissa, D.H., Shinjo, R., Kitagawa, H., Meshesha, D., Nakamura, E., 2017. Petrologic and geochemical characterization of rift-related magmatism at the northernmost Main Ethiopian Rift: Implications for plume-lithosphere interaction and the evolution of rift mantle sources. Lithos 282-283, 240–261. https://doi.org/10.1016/j.lithos.2017.03.011.

Field, L., Blundy, J., Brooker, R.A., Wright, T., Yirgu, G., 2012. Magma storage conditions beneath Dabbahu Volcano (Ethiopia) constrained by petrology, seismicity and satellite geodesy. Bull. Volcanol. 74 (5), 981–1004. https://doi.org/10.1007/s00445-012-0580-6.

Field, L., Blundy, J., Calvert, A., Yirgu, G., 2013. Magmatic history of Dabbahu, a composite volcano in the Afar Rift, Ethiopia. Geological Society of America Bulletin 125 (1–2), 128–147. https://doi.org/10.1130/b30560.1.

Fitton, J.G., Saunders, A.D., Norry, M.J., Hardarson, B.S., Taylor, R.N., 1997. Thermal and chemical structure of the Iceland plume. Earth Planet. Sci. Lett. 153 (3–4), 197–208. https://doi.org/10.1016/S0012-821X(97)00170-2.

Gündüz, M., Asan, K., 2021. PetroGram: an excel-based petrology program for modeling of magmatic processes. Geosci. Front. 12 (1), 81–92. https://doi.org/10.1016/j.gsf.2020.06.010.

Hammond, J.O.S., Kendall, J.M., Stuart, G.W., Keir, D., Ebinger, C., Ayele, A., Belachew, M., 2011. The nature of the crust beneath the Afar triple junction: evidence from receiver functions. Geochem. Geophys. Geosyst. 12 (12), n/a–n/a. https://doi.org/10.1029/2011gc003738.

Hart, S.R., 1984. A large-scale isotope anomaly in the Southern Hemisphere mantle. Nature 309 (5971), 753–757. https://doi.org/10.1038/309753a0.

Hofmann, A.W., White, W.M., 1982. Mantle plumes from ancient oceanic crust. Earth Planet. Sci. Lett. 57 (2), 421–436. https://doi.org/10.1016/0012-821X(82)90161-3.

Hofmann, A.W., Jochum, K.P., Seufert, M., White, W.M., 1986. Nb and Pb in oceanic basalts: new constraints on mantle evolution. Earth Planet. Sci. Lett. 79, 33–45. https://doi.org/10.1016/0012-821X(86)90038-5.

Hofmann, C., Courtillot, V., Féraud, G., Rochette, P., Yirgu, G., Ketefo, E., Pik, R., 1997. Timing of the Ethiopian flood basalt event and implications for plume birth and global change. Nature 389 (6653), 838–841. https://doi.org/10.1038/39853.

Hofstetter, R., Beyth, M., 2003. The Afar Depression: interpretation of the 1960-2000 earthquakes. Geophys. J. Int. 155 (2), 715–732. https://doi.org/10.1046/j.1365-246x.2003.02080.x.

Hutchison, W., Mather, T.A., Pyle, D.M., Boyce, A.J., Gleeson, M.L.M., Yirgu, G., Blundy, J.D., Ferguson, D.J., Vye-Brown, C., Millar, I.L., Sims, K.W.W., Finch, A.A.,

2018. The evolution of magma during continental rifting: New constraints from the isotopic and trace element signatures of silicic magmas from Ethiopian volcanoes. Earth Planet. Sci. Lett. 489, 203–218. https://doi.org/10.1016/j.epsl.2018.02.027.

Illsley-Kemp, F., Keir, D., Bull, J.M., Gernon, T.M., Ebinger, C., Ayele, A., Hammond, J.O. S., Kendall, J.M., Goitom, B., Belachew, M., 2018. Seismicity during Continental Breakup in the Red Sea Rift of Northern Afar. Journal of Geophysical Research: Solid Earth 123 (3), 2345–2362. https://doi.org/10.1002/2017jb014902.

Irvine, T.N., Baragar, W.R.A., 1971. A guide to the chemical classification of the common volcanic rocks. Can. J. Earth Sci. 8 (5), 523–548. https://doi.org/10.1139/e71-055.

Jackson, M.G., Dasgupta, R., 2008. Compositions of HIMU, EM1, and EM2 from global trends between radiogenic isotopes and major elements in ocean island basalts. Earth Planet. Sci. Lett. 276 (1–2), 175–186. https://doi.org/10.1016/j.epsl.2008.09.023.

Jackson, M.G., Hart, S.R., Konter, J.G., Kurz, M.D., Blusztajn, J., Farley, K.A., 2014. Helium and lead isotopes reveal the geochemical geometry of the Samoan plume. Nature 514 (7522), 355–358. https://doi.org/10.1038/nature13794.

Kamber, B.S., Gladu, A.H., 2009. Comparison of Pb Purification by Anion-Exchange Resin Methods and Assessment of Long-Term Reproducibility of Th/U/Pb Ratio Measurements by Quadrupole ICP-MS. Geostand. Geoanal. Res. 33 (2), 169–181. https://doi.org/10.1111/j.1751-908x.2009.00911.x.

Lahitte, P., Gillot, P.-Y., Courtillot, V., 2003. Silicic central volcanoes as precursors to rift propagation: the Afar case. Earth Planet. Sci. Lett. 207 (1–4), 103–116. https://doi.org/10.1016/s0012-821x(02)01130-5.

Lalou, C., Van Nguyen, H., Faure, H., Moreira, L., 1970. Datation par la méthode Uranium-Thorium des hauts niveaux de coraux de la dépression de l'Afar (Éthiopie). Rev. Géol. Dynam. Géog. Phys. 12 (1), 3–8.

Lavayssiere, A., Rychert, C., Harmon, N., Keir, D., Hammond, J.O.S., Kendall, J.M., Doubre, C., Leroy, S., 2018. Imaging Lithospheric Discontinuities beneath the Northern East African Rift using S-to-P Receiver Functions. Geochem. Geophys. Geosyst. 19 (10), 4048–4062. https://doi.org/10.1029/2018GC007463.

LeBas, M.J., Le Maitre, R.W., Streckeisen, A., Zanettin, B., IUGS Subcommission on the Systematics of Igneous Rocks, 1986. A chemical classification of volcanic rocks based on the total alkali-silica diagram. J. Petrol. 27 (3), 745–750. https://doi.org/10.1093/petrology/27.3.745.

Lee, C.-T.A., Luffi, P., Plank, T., Dalton, H., Leeman, W.P., 2009. Constraints on the depths and temperatures of basaltic magma generation on Earth and other terrestrial planets using new thermobarometers for mafic magmas. Earth Planet. Sci. Lett. 279 (1–2), 20–33. https://doi.org/10.1016/j.epsl.2008.12.020.

Leroy, S., Razin, P., Autin, J., Bache, F., D'Acremont, E., Watremez, L., Robinet, J., Baurion, C., Denèle, Y., Bellahsen, N., Lucazeau, F., Rolandone, F., Rouzo, S., Kiel, J. S., Robin, C., Guillocheau, F., Tiberi, C., Basuyau, C., Beslier, M.-O., et al., 2012. From rifting to oceanic spreading in the Gulf of Aden: a synthesis. Arab. J. Geosci. 5 (5), 859–901. https://doi.org/10.1007/s12517-011-0475-4.

Lewi, E., Keir, D., Birhanu, Y., Blundy, J., Stuart, G., Wright, T., Calais, E., 2016. Use of a high-precision gravity survey to understand the formation of oceanic crust and the role of melt at the southern Red Sea rift in Afar, Ethiopia. Geol. Soc. Lond., Spec. Publ. 420 (1), 165–180. https://doi.org/10.1144/sp420.13.

Maguire, P.K.H., Keller, G.R., Klemperer, S.L., Mackenzie, G.D., Keranen, K., Harder, S., O'Reilly, B., Thybo, H., Asfaw, L., Khan, M.A., Amha, M., 2006. Crustal structure of the northern Main Ethiopian Rift from the EAGLE controlled-source survey; a snapshot of incipient lithospheric break-up. In: Yirgu, G., Ebinger, C., Maguire, P.K. H. (Eds.), The Afar Volcanic Province within the East African Rift System, vol. 259. Geological Society, London, pp. 269–292. https://doi.org/10.1144/GSL.SP.2006.259.01.21. Special Publications.

Mahatsente, R., Jentzsch, G., Jahr, T., 1999. Crustal structure of the Main Ethiopian Rift from gravity data: 3-dimensional modeling. Tectonophysics 313, 363–382. https://doi.org/10.1016/S0040-1951(99)00213-9.

Makris, J., Ginzburg, A., 1987. The Afar Depression: transition between continental rifting and sea-floor spreading. Tectonophysics 141 (1–3), 199–214. https://doi.org/10.1016/0040-1951(87)90186-7.

Mana, S., Furman, T., Carr, M.J., Mollel, G.F., Mortlock, R.A., Feigenson, M.D., Turrin, B. D., Swisher, C.C., 2012. Geochronology and geochemistry of the Essimingor volcano: Melting of metasomatized lithospheric mantle beneath the North Tanzanian Divergence zone (East African Rift). Lithos 155, 310–325. https://doi.org/10.1016/j.lithos.2012.09.009.

McDonough, W.F., Sun, S., 1995. The composition of the Earth. Chem. Geol. 120, 223–253. https://doi.org/10.1016/0009-2541(94)00140-4.

Medynski, S., Pik, R., Burnard, P., Williams, A., Vye-Brown, C., Ferguson, D., Blard, P.H., France, L., Yirgu, G., Seid, J.I., Ayalew, D., Calvert, A., 2013. Controls on magmatic cycles and development of rift topography of the Manda Hararo segment (Afar, Ethiopia): Insights from cosmogenic 3He investigation of landscape evolution. Earth Planet. Sci. Lett. 367, 133–145. https://doi.org/10.1016/j.epsl.2013.02.006.

Medynski, S., Pik, R., Burnard, P., Vye-Brown, C., France, L., Schimmelpfennig, I., Whaler, K., Johnson, N., Benedetti, L., Ayelew, D., Yirgu, G., 2015. Stability of rift axis magma reservoirs: Spatial and temporal evolution of magma supply in the Dabbahu rift segment (Afar, Ethiopia) over the past 30 kyr. Earth Planet. Sci. Lett. 409, 278–289. https://doi.org/10.1016/j.epsl.2014.11.002.

Niu, Y., 2021. Lithosphere thickness controls the extent of mantle melting, depth of melt extraction and basalt compositions in all tectonic settings on Earth–a review and new perspectives. Earth Sci. Rev. 217, 103614 https://doi.org/10.1016/j.earscirev.2021.103614.

Pagli, C., Wright, T.J., Ebinger, C.J., Yun, S.-H., Cann, J.R., Barnie, T., Ayele, A., 2012. Shallow axial magma chamber at the slow-spreading Erta Ale Ridge. Nat. Geosci. 5 (4), 284–288. https://doi.org/10.1038/ngeo1414.

Phipps Morgan, J., Chen, Y., 1993. Dependence of ridge-axis morphology on magma supply and spreading rate. Nature 364, 706–708. https://doi.org/10.1038/364706a0.

Pik, R., Deniel, C., Coulon, C., Yirgu, G., Marty, B., 1999. Isotopic and trace element signatures of Ethiopian flood basalts: evidence for plume–lithosphere interactions. Geochimica et Cosmochimica Acta. Geochimica et Cosmochimica Acta (63), 2263–2279. https://doi.org/10.1016/S0016-7037(99)00141-6.

Pin, C., Briot, D., Bassin, C.P., Franck., 1994. Concomitant separation of strontium and samarium-neodymium for isotopic analysis in silicate samples, based on specific extraction chromatography. Alaytica Chimica Acta 298 (2), 209–217. https://doi.org/10.1016/0003-2670(94)00274-6.

Rooney, T.O., 2017. The Cenozoic magmatism of East-Africa: part I — Flood basalts and pulsed magmatism. Lithos 286-287, 264–301. https://doi.org/10.1016/j.lithos.2017.05.014.

Rooney, T.O., 2020a. The Cenozoic magmatism of East Africa: Part II – Rifting of the mobile belt. Lithos 360-361. https://doi.org/10.1016/j.lithos.2019.105291.

Rooney, T.O., 2020b. The Cenozoic magmatism of East Africa: Part IV – the terminal stages of rifting preserved in the Northern East African Rift System. Lithos 360-361. https://doi.org/10.1016/j.lithos.2020.105381.

Rooney, T.O., 2020c. The Cenozoic magmatism of East Africa: Part V – Magma sources and processes in the East African Rift. Lithos 360–361. https://doi.org/10.1016/j.lithos.2019.105296.

Rooney, T.O., Hanan, B.B., Graham, D.W., Furman, T., Blichert-Toft, J., Schilling, J.-G., 2012. upper mantle pollution during Afar Plume–Continental rift interaction. J. Petrol. 53 (2), 365–389. https://doi.org/10.1093/petrology/egr065.

Siegburg, M., Gernon, T.M., Keir, D., Bull, J.M., Taylor, R.N., Watts, E.J., Greenfield, T., Gebru, E.F., 2023. Temporal clustering of fissural eruption across multiple segments within the Ethiopian Rift. Front. Earth Sci. 11 https://doi.org/10.3389/feart.2023.1169635.

Stracke, A., Hofmann, A.W., Hart, S.R., 2005. FOZO, HIMU, and the rest of the mantle zoo. Geochem. Geophys. Geosyst. 6 (5) https://doi.org/10.1029/2004gc000824.

Su, B., Zhang, H., Asamoah, S.P., Qin, K., Tang, Y., Ying, J., Xiao, Y., 2010. Garnet-spinel transition in the upper mantle: Review and interpretation. J. Earth Sci. 21 (5), 635–640. https://doi.org/10.1007/s12583-010-0117-x.

Sun, S., McDonough, W.F., 1989. Chemical and isotopic systematics of oceanic basalts: implications for mantle composition and processes. Geol. Soc. Lond., Spec. Publ. 42 (1), 313–345. https://doi.org/10.1144/GSL.SP.1989.042.01.19.

Taylor, R.N., Ishizuka, O., Michalik, A., Milton, J.A., Croudace, I.W., 2015. Evaluating the precision of Pb isotope measurement by mass spectrometry. J. Anal. At. Spectrom. 30 (1), 198–213. https://doi.org/10.1039/c4ja00279b.

Taylor, R.N., Davila-Harris, P., Branney, M.J., Ruth Farley, E.M., Gernon, T.M., Palmer, M.R., 2020. Dynamics of a chemically pulsing mantle plume. Earth Planet. Sci. Lett. 537 https://doi.org/10.1016/j.epsl.2020.116182.

Teklay, M., Scherer, E.E., Mezger, K., Danyushevsky, L., 2010. Geochemical characteristics and Sr–Nd–Hf isotope compositions of mantle xenoliths and host basalts from Assab, Eritrea: implications for the composition and thermal structure of the lithosphere beneath the Afar Depression. Contrib. Mineral. Petrol. 159, 731–751. https://doi.org/10.1007/s00410-009-0451-0.

Tortelli, G., Gioncada, A., Pagli, C., Rosi, M., De Dosso, L., Keir, D., 2021. Evidence of active magmatic rifting at the Ma'Alalta volcanic field (Afar, Ethiopia). Bull. Volcanol. 83 (6) https://doi.org/10.1007/s00445-021-01461-4.

Tortelli, G., Gioncada, A., Pagli, C., Braschi, E., Gebru, E.F., Keir, D., 2022. Constraints on the Magma Source and Rift Evolution from Geochemistry of the Stratoid Flood Basalts (Afar, Ethiopia). Geochem. Geophys. Geosyst. 23 (8) https://doi.org/10.1029/2022gc010434.

Vidal, P., Deniel, C., Vellutini, P.J., Piguet, P., Coulon, C., Vincent, J., Audin, J., 1991. Changes of mantle sources in the course of a rift evolution: the Afar Case. Geophys. Res. Lett. 18 (10), 1913–1916. https://doi.org/10.1029/91gl02006.

Viltres, R., Jónsson, S., Ruch, J., Doubre, C., Reilinger, R., Floyd, M., Ogubazghi, G., 2020. Kinematics and deformation of the southern Red Sea region from GPS observations. Geophys. J. Int. 221 (3), 2143–2154. https://doi.org/10.1093/gji/ggaa109.

Volker, F., McCulloch, M.T., Altherr, R., 1993. Submarine basalts from the Red Sea: new Pb, Sr, and Nd isotopic data. Geophys. Res. Lett. 20 (10), 927–930. https://doi.org/10.1029/93GL00050.

Watts, E.J., Gernon, T.M., Taylor, R.N., Keir, D., Siegburg, M., Jarman, J., Pagli, C., Gioncada, A., 2020. Evolution of the Alu-Dalafilla and Borale volcanoes, Afar, Ethiopia. J. Volcanol. Geotherm. Res. 408 https://doi.org/10.1016/j.jvolgeores.2020.107094.

Wolfenden, E., Ebinger, C., Yirgu, G., Deino, A., Ayalew, D., 2004. Evolution of the northern Main Ethiopian rift: birth of a triple junction. Earth Planet. Sci. Lett. 224 (1–2), 213–228. https://doi.org/10.1016/j.epsl.2004.04.022.

Wolfenden, E., Ebinger, C., Yirgu, G., Renne, P.R., Kelley, S.P., 2005. Evolution of a volcanic rifted margin: Southern Red Sea, Ethiopia. Geological Society of America Bulletin 117 (7), 846. https://doi.org/10.1130/b25516.1.

Woodhead, J.D., 1996. Extreme HIMU in an oceanic setting: the geochemistry of Mangaia Island (Polynesia), and temporal evolution of the Cook—Austral hotspot. J. Volcanol. Geotherm. Res. 72, 1–19. https://doi.org/10.1016/0377-0273(96)00002-9.

Wright, T.J., Sigmundsson, F., Pagli, C., Belachew, M., Hamling, I.J., Brandsdóttir, B., et al., 2012. Geophysical constraints on the dynamics of spreading centres from rifting episodes on land. Nat. Geosci. 5 (4), 242–250. https://doi.org/10.1038/ngeo1428.